ANNALS OF GEOPHYSICS, 68, 6, S684, 2025; doi:10.4401/ag-9357
OPEN ACCESS

Numerical Seismic Hazard Assessment for the San Ramón Fault Using Heterogeneous Energy-Based Kinematic Simulations

Patricio Venegas-Aravena[*,1]

(1) Universidad Loyola Andalucía, Department of Engineering, Seville, Spain

Article history: received April 27, 2025; accepted September 15, 2025

Abstract

Conventional earthquake simulations, employing computationally efficient but simplified homogeneous parameters, often yield unrealistic runaway ruptures and inaccurate ground motion predictions. Conversely, dynamic rupture simulations and large earthquakes reveal a strong correlation between accumulated energy and final rupture distribution, demonstrating that energy constraints significantly reduce seismic source uncertainties. Therefore, realistic rupture analyses should prioritize energy-constrained, heterogeneous models over probabilistic methods for seismic hazards analysis. This necessitates simulations incorporating fault heterogeneities and geometries, as demonstrated by the Heterogeneous Energy-Based kinematic method. This recent perspective is particularly relevant for faults near urban areas such as the San Ramón fault which is located near the city of Santiago (Chile) and potentially impacting 6.5 million people. When considering ground motion amplifications, it is obtained a ground motion greater than expected for a magnitude 6.5 event, suggesting that the city could experience peak ground acceleration (PGA) values greater than 0.6 g at 10 km from the fault. The city would face maximum accelerations close to 0.9 g. PGA values close to critical structures, such as the 'La Reina' nuclear reactor, hospitals and the country's government center, show accelerations higher than those recorded by the Fukushima-Daiichi reactor during the 2011 Tohoku earthquake.

Keywords: Self-arrested rupture simulation; Ground motion amplification; Peak ground acceleration (PGA); San Ramon Fault; Heterogeneous rupture parameters

1. Introduction

Numerical models can be used to predict ground motion from earthquakes by modeling the behavior of seismic ruptures, the process through which energy is released along a geological fault. These simulations can estimate the earthquake magnitude, the distribution of seismic energy, and ground motion at various locations near the epicenter. Information derived from both the seismic source and ground shaking is relevant for estimating the potential damage that an earthquake could cause to urban areas, infrastructure, and other sites of interest (Honoré et al., 2011; Paolucci et al., 2014; Rezaeian and Sun, 2014; Taborda and Roten, 2015; De Matteis and Zizi, 2018; Mourhatch and

Krishnan, 2020; Wang et al., 2021; Bommer et al., 2022; Glehman and Tsesarsky, 2022; Nweke et al., 2022). Seismic hazard analysis benefits greatly from rupture models that closely replicate natural earthquake behavior, particularly when incorporating fault geometry and heterogeneous rupture conditions. These heterogeneities are essential for accurately simulating strong ground motions (e.g. Aochi and Ide, 2014; Bradley et al., 2017a; Bradley et al., 2017b; Wang et al., 2021; Oral et al., 2022; Song and Duan, 2023; Melgar et al., 2023). For example, simulations that incorporate fault complexities reveal high corner frequency zones that are absent in simpler models (e.g. Schliwa and Gabriel, 2023; Venegas-Aravena, 2023a).

A particularly significant observation is that computational dynamic rupture simulations and analyses of large-magnitude earthquakes consistently reveal a strong spatial correlation between pre-rupture accumulated energy and the resultant rupture distribution (e.g. Moreno et al., 2010; Venegas-Aravena et al., 2024). This empirical finding suggests that the inherent complexity of the rupture process, when rigorously constrained by the availability of energy, leads to a substantial reduction in both uncertainties and epistemic errors that are typically associated with rupture modeling. In addition, a recent finding by Venegas-Aravena and Zaccagnino (2025) indicates that earthquakes tend to exhibit more deterministic behavior as their magnitude increases. This implies that, unlike smaller events, the rupture propagation of large earthquakes is less random and is instead more strongly controlled by the physical characteristics and large-scale geometry of the fault. Consequently, it is advocated that rupture analyses should prioritize the implementation of physically realistic conditions governed by energy constraints, as opposed to relying on probabilistic methodologies that frequently fail to adequately represent the heterogeneous nature of rupture phenomena. Therefore, comprehending the complexity of spatial variability in rupture parameters is fundamental for seismic wave propagation. For instance, natural earthquakes typically demonstrate slip distributions that follow a power-law relationship, implying that a small number of areas experience significant slip, while the majority of the fault surface undergoes relatively minor displacement (Somerville et al., 1999; Venegas-Aravena, 2023b). This feature of the rupture process can also be related to energy release, which is known as the asperity criterion (Somerville et al., 1999). Specifically, this criterion states that between a quarter and a third of the rupture zone releases nearly half of the seismic moment. This criterion has been tested for crustal earthquakes and is also used to constrain rupture scenarios (Kagawa et al., 2004; Li et al., 2024; Shimmoto, 2024). Basically, this criterion demonstrates that real ruptures are fundamentally heterogeneous, partitioning faults into high and low-slip segments. This uneven energy release, concentrated in "asperities," directly controls the high-frequency content and directivity of ground motion. By requiring models to reproduce this heterogeneous distribution, the criterion ensures simulations are statistically equivalent to real-world earthquakes (Venegas-Aravena et al., 2024), improving the accuracy of seismic hazard assessments. Then, the asperity criterion is a crucial physical test for validating numerical earthquake models. Nevertheless, this fundamental feature is not tested often because it is difficult to obtain, as it requires that rupture simulations be stopped before the rupture reaches the edges of the fault. For example, dynamic simulations demonstrate that the asperity criterion breaks down at fault edges, indicating independent rupture parameter evolution. This contrasts with self-arrested simulations, where parameters exhibit higher correlations and satisfy the asperity criterion (Venegas-Aravena et al., 2024). In this context, the kinematic heterogeneous Energy-Based method (HE-B method), proposed by Venegas-Aravena (2023), suggests a way to obtain this type of heterogeneous ruptures that meet this roughness criterion. This method assumes that the spatial variability of rupture parameters, such as final slip or rupture velocity, is strongly related to the residual energy, which is defined as the difference between the available energy and the fracture energy (Noda et al., 2022). Consequently, parameters such as rupture velocity, final slip, and residual energy tend to decrease towards the edges of the rupture. This HE-B method creates distinct, localized zones of high slip and energy release (the asperities) and allows the rupture to naturally "arrest" instead of propagating unrealistically. This is a crucial distinction from traditional simulations that often fail to incorporate this physical requirement.

Several authors have suggested that fracture energy may be related to fault roughness (Ohnaka, 2013), implying that parameters such as toughness and fracture energy increase as the rupture progresses into fault sections with steeper dips (Lung, 1985; Smith, 1986). This implies that frictional parameters depend directly on the fractal geometry of the fault (Heping, 1989; Herrera et al., 2023). Besides, it has been found that geometric and frictional variations among different sections within faults generate greater variability in ground motion (Strasser and Bommer, 2009). Therefore, incorporating fault heterogeneities and geometry into simulations is expected to yield more reliable predictions of strong ground motion compared to models that do not account for such features. This is because considering physical processes such as the spatial variability of fracture energy helps to better model strong ground motion (Panza et al., 2004). This becomes particularly relevant when assessing the potential

damage that ground motion can cause in urban areas, especially when fault lines are in proximity. Here is crucial to note that both the rupture propagation modeled by the HE-B method and the seismic wave propagation described by the analytical equations of Aki and Richards (1980) are deterministic models designed to capture the essential aspects of seismicity using well-established physical principles and experimental data. The introduction of epistemic uncertainty, which reflects the limitations of our knowledge, could undermine the deterministic nature of the model by challenging the physical validity of the rupture processes. Moreover, when data availability is limited quantifying such uncertainties becomes problematic.

In this context, the present study aims to delineate high ground acceleration zones near urban areas using the HE-B method, considering the geometric irregularities of fault lines with no epistemic analysis. Specifically, the focus is on the active San Ramón fault, which traverses from north to south through the Santiago basin in Chile and is part of the western Andean thrust front (WATF) (Maldonado et al., 2021). Santiago is the country's largest city, with a population of approximately 6 million people, and serves as the capital (Yáñez et al., 2015). Furthermore, it serves as the nation's administrative and economic hub, making any potential damage to the city a matter of national concern. Given the recent urban expansion over the fault, accurate fault characterization is crucial for assessing the potential damage it could cause. For instance, the San Ramón fault is a reverse fault with a length of approximately 25 km from north to south, of which its northern section (around 10 km) traverses the eastern sector of the city (Armijo et al., 2010). It's essential to highlight that paleo seismic studies have indicated that this fault has the potential to generate earthquakes with a magnitude close to M_w 7 and a slip of several meters (Vargas et al., 2014). Due to its proximity to a major metropolitan area, such an event could lead to significant devastation. The main objective of this study is to produce a map estimating the maximum ground accelerations for the city of Santiago by creating a heterogeneous rupture scenario with geometric considerations using the HE-B method for the San Ramón fault. Note that "heterogeneous" in this context refers to the absence of any parameter uniformly distributed across the fault. That's why in Section 2, the properties of San Ramon Fault and Santiago Basin are presented. In Section 3 we provide a description of the HE-B method and the heterogeneous energy conditions required to generate a rupture in the San Ramón Fault. A rupture scenario is presented in Section 4, while ground motion is discussed in Section 5. The summary and discussion are found in Section 6, and the conclusions are presented in Section 7.

2. The San Ramón Fault and Santiago Basin

The San Ramón fault is located in the central Andes Mountain range, at a latitude of approximately 33°30'S and a longitude of 70°30'W (Fig. 1a and b). It spans approximately 25 km, as indicated in red in Fig. 1b. Additionally, this figure displays the urban area of Santiago (black curve) along with major roads (yellow and gray curves). The symbols in Fig. 1b also denote the locations of various points of interest, such as the 'La Reina' nuclear research center, which houses an experimental nuclear reactor and is near the fault (orange triangle in Fig. 1b) (https://www.cchen.cl/?page_id=156). The squares, star, and circle in this figure represent other points of interest like hospitals, the country's administrative center, and universities (Table 1). The fault has a dip angle ranging from 45 to 55 degrees and extends from the surface to a depth of approximately 11 km (Riesner et al., 2017). The color map in Fig. 1b shows an approximate distribution of ground motion amplification due to sedimentary deposits, based on the work developed by Pilz et al. (2011). This approximation highlights four major amplification zones within the urban area of Santiago. These zones of higher amplitude were modeled using combinations of two-dimensional Gaussian functions (see code availability section), providing a simplified yet representative distribution. This approach helps preserve the primary amplification features while avowing unnecessary resolution detail that may not significantly affect the overall results. The first relevant zone is characterized by a higher amplification in the westernmost sector, with values greater than 70%. A similar pattern is observed in the western part of the third zone. Meanwhile, zones 2 and 4 exhibit slightly lower amplification values, generally above 30%. The presence of these large sedimentary deposits, which generate significant ground amplification, in the westernmost zone of the Santiago basin has been confirmed by more recent studies (Yañez et al., 2015).

Figure 1c provides a three-dimensional view of the fault. Additional information about the fault is available through the "Fallas de Chile" project (https://fallasdechile.ing.uc.cl/). It's important to note that the fault has low resolution, and spatial noise has been added to it. For instance, when data points are available at 500 meter intervals, it is possible to interpolate a smoother fault surface that follows a defined distribution. As faults tend

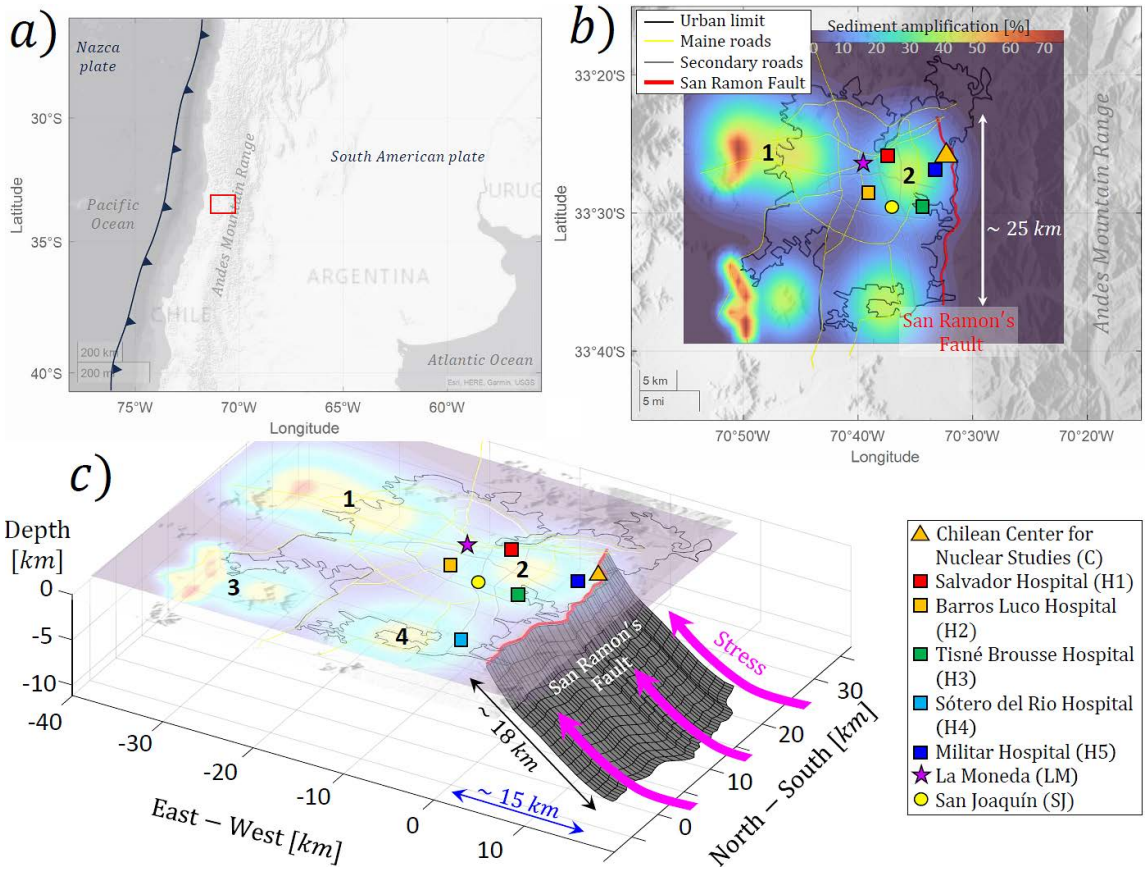

Figure 1. Location and Key Geometric Features of the San Ramón Fault. The red rectangle in (a) indicates the fault's location. (b) provides an enlarged view of the red zone from (a), with the fault depicted in red. Infrastructure of interest, such as major roads (yellow and gray lines), and critical facilities, including hospitals (colored squares), the government center (star), the nuclear reactor (triangle), and the Catholic University (circle), are also shown. Further details are presented in Table 1. The color map shows the percentage amplification of strong motion (PGA and PGV) due to the presence of sediments in the Santiago basin (based on the work of Pilz et al., 2011). (c) displays the fault's geometry in a three-dimensional view.

to be described by power-law distributions (Okubo and Aki, 1987; Candela et al., 2012), data can be interpolated to obtain values approximately every ~60 meters for strike and ~90 meters for dip, respectively (see Table 2), using the code developed by Chen and Yang (2016). A one-dimensional schematic representation is shown in Fig. 2a.

3. Estimating Fracture Energy and Residual Energy in the San Ramon Fault

Emphasizing fault geometry is particularly relevant to the Heterogeneous Energy-Based (HE-B) method, as it relies on the spatial distributions of available energy ΔW_0 and fracture energy G_C, which can be directly related to fault geometry (Ohnaka, 2013; Venegas-Aravena, 2023b; Venegas-Aravena and Cordaro, 2023). In particular, the HE-B method establishes that areas capable of fracturing must have positive residual energy E^{res}, defined as the difference between available energy and fracture energy (Noda et al., 2022). This condition is:

$$E^{res} = \Delta W_0 - G_C \tag{1}$$

It is important to emphasize that this equation, in the context of the HE-B method, is valid for every point within the fault and defines the rupture area, ensuring that there must be a decrease in the values of E^{res} towards

the rupture edges, where it reaches zero. The HE-B method operates by first defining a heterogeneous distribution of available energy across a fault plane, with values decreasing towards the edges. This energy distribution is based on the empirical aspect ratios of real earthquakes as defined by Leonard (2010). The method ensures a realistic rupture process by setting the area with the highest residual energy (available energy minus fracture energy) as the rupture initiation point. From this central high-energy zone, the rupture propagates outwards. As it moves toward the low-energy boundaries, rupture parameters like rupture velocity v_r, final slip u_f, and slip velocity naturally decrease, leading to a realistic, self-arresting event. That is $u_f = u_f(E^{res})$ and $v_r = v_r(E^{res})$ (Venegas-Aravena, 2023b). This procedure inherently creates concentrated high-slip "asperities" within a larger area of lower slip, thus ensuring the heterogeneity of the rupture process – a key feature often missing in other numerical models.

In this regard, Eq. (1) becomes a constraint on the rupture's evolution, as it physically implies that low values of u_f and v_r towards the rupture edge are associated with a reduced amount of available energy, an increase in dissipation, or both. That is, Eq. (1) tells us that those areas of the fault where ΔW_0 is greater than G_C are the only ones with the potential to generate seismicity. Conversely, as G_C increases, the fault tends to have lower values of residual energy and, therefore, comes to a halt. Since both G_C and ΔW_0 are defined pointwise on the fault, they can be non-constant (or non-uniform) on the fault. That is, they have spatial variability. In the case shown by Venegas-Aravena (2023b), these distributions do not evolve temporally since they are considered as necessary inputs to constrain the kinematic parameters that do evolve both spatially and temporally. Specifically, the final slip is constrained by the residual energy, but the evolution of the slip rate at each point on the fault is determined by a truncated Yoffe function. This function is the convolution of a normal Yoffe function with a triangular function, which was defined as 1.5 times dt (Tinti et al., 2005; Venegas-Aravena, 2023b). The time when the rupture begin is determined as the inverse of the rupture velocity ($v_r \sim 1/\nabla t_r$), which is proportional to the residual energy (Venegas-Aravena, 2023b).

Table 1. Geographical Location of Points of Interest Marked in Fig. 1b and c, Corresponding to Critical Infrastructure Near the San Ramón Fault. Maximum ground velocities and accelerations are shown for each infrastructure.

Location	(Lat, Lon)	PGV (m/s)	PGV-sediments (m/s)	PGA (g)	PGA-sediments (g)
Chilean center for nuclear studies (C)	−33.428, −70.525	0.3585	0.4044	0.6754	0.7619
Hospital del Salvador (H1)	−33.436, −70.625	0.3162	0.4017	0.5049	0.6415
Hospital Barros Luco (H2)	−33.484, −70.646	0.4081	0.4734	0.5963	0.6917
Hospital Tisné Brousse (H3)	−33.501, −70.579	0.4139	0.5016	0.6612	0.8013
Hospital Sótero del Rio (H4)	−33.577, −70.581	0.4144	0.4897	0.6453	0.7626
Hospital Militar (H5)	−33.450, −70.538	0.3554	0.4577	0.6356	0.8186
La Moneda (LM)	−33.443, −70.653	0.2726	0.3092	0.4098	0.4648
San Joaquin (SJ)	−33.499, −70.613	0.3644	0.4352	0.4966	0.6917

In geometric terms, G_C increases when the surface is rougher (Venegas-Aravena and Cordaro, 2023), indicating that there can be abrupt changes in angles between different fault segments. This means that a rougher fault surface (one with a greater inclination angle between adjacent segments) requires more energy to propagate a rupture. This is because a rougher fault surface means there is more geometric irregularities and a greater contact area per unit of rupture length (compared to smooths faults). To propagate the rupture, the earthquake must overcome the friction and physical obstacles presented by these irregularities. This makes the fault more resistant to fracture and rupture propagation. Therefore, areas with greater fault roughness can act as barriers to a propagating rupture,

influencing the final size and slip distribution of an earthquake. Indeed, there are relationships between the surface's inclination angle α and G_C (A schematic representation of a rupture propagating along a fault with a given inclination defined by an angle θ is depicted in Fig. 2b). For example, the variation of the fracture energy G_C in terms of the angle is given by (page 328 in Xie, 1993):

$$G_C = G_{C0} 10^{log(3) - log\left(2cos\left(\frac{\alpha}{2}\right)\right)} \tag{2}$$

Where α is the angle in radians (in degrees $\theta = \alpha\, 180/\pi$) and G_{C0} is the reference (material) fracture energy. Note that Xie (1993) performs this analysis in terms of the fracture toughness K, which can be related to G_C as $K/K_0 = \sqrt{G_C/G_{C0}}$ where K_0 is the reference fracture toughness. The ratio between G_C and G_{C0} as described in Eq. (2) is shown in the black curve in Fig. 2c. It can be observed that larger angles result in an increase in G_C, with G_C being more than 1.7 times greater than G_{C0} for inclination angles on the order of 60 degrees. Figure 2c also illustrates that the increase in G_C as a function of the angle α is approximately quadratic. This suggests that fault roughness can lead to an increase in fracture energy, resulting in less energy available for slip, which is consistent with more recent analyses of self-similar surfaces (Fang and Dunham, 2013). Surfaces exhibiting greater roughness are also less prone to rupture initiation due to less localized stress (Venegas-Aravena et al., 2022) leading to the extended time required for the accumulation of energy necessary to induce failure (Venegas-Aravena, 2025).

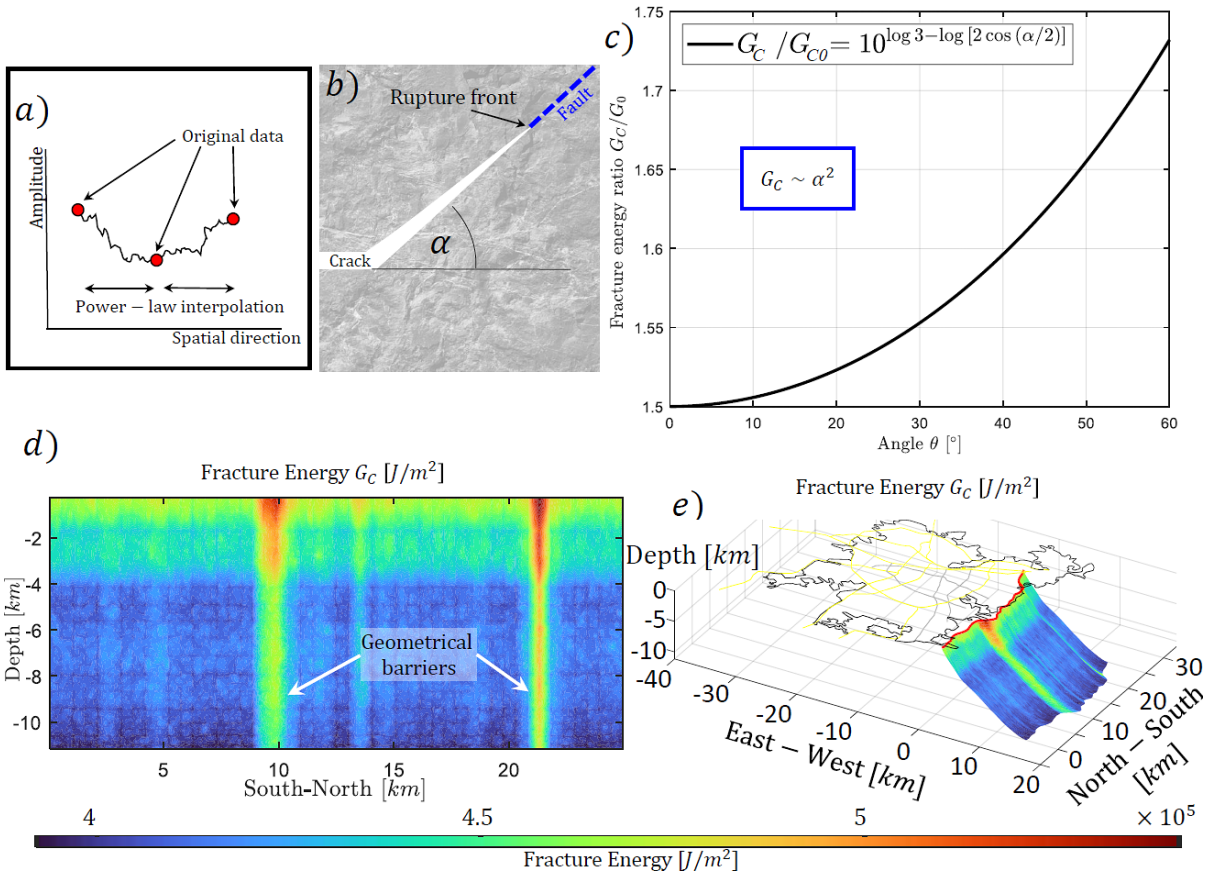

Figure 2. (a) A representation of interpolation between various data points (red dots) is shown. The black curve corresponds to the curve created among data points that follow a power-law distribution, which is typical in faults. (b) A schematic of a rupture changing angle as it propagates. (c) Change in the aspect ratio between G_C and G_{C0} as the fault angle or roughness increases, as described by Eq. (2). (d) Fracture energy of the San Ramón fault using G_{C0} for the sandstone (Vora and Morgan, 2019). An increase in G_C is observed as the fault becomes shallower, along with two vertical strips of high G_C, indicating the presence of geometric barriers in the north-south direction. (e) Three-dimensional view of fracture energy in the San Ramón fault.

When considering Eq. (2) in the geometrical irregularities (in dip and strike) of the San Ramón fault and $G_{C0} = 1.3 \times 10^5$ J/m^2 for the sandstone (Vora and Morgan, 2019) identified in this region (Araya et al., 2021), it is observed that G_C varies significantly with depth. Figure 2d illustrates those lower values of G_C are located in the deepest part of the fault (shades of blue and dark blue). Conversely, higher values of G_C are concentrated in the shallow zone of the fault (shades of green in Fig. 2d) and in two bands that extend from the shallow zone towards the deeper regions, approximately at 10 km and 22 km in the north-south direction. Within these bands, the highest G_C values are also found in the shallowest areas (shades of red in Fig. 2d). The minimum and maximum values of G_C are ~3.9×10^5 J/m^2 and ~5.45×10^5 J/m^2, respectively. The average G_C value is ~0.42 MJ/m^2. Considering an average stress drop of approximately 3 MPa and $G_C = 0.5\Delta\tau \times D_C$, this yields an average critical distance D_C of approximately 0.3 m, which falls within the commonly reported range (e.g. Tinti et al., 2009). This demonstrates that, for a real fault, G_C values are not constant but can exhibit significant variations within the same fault. Here is also important to note that Eq. (2) is dependent on the geometric variation of the fault; therefore, the initial value of fracture energy is merely referential, as it will not alter the final spatial distribution thereof. Figure 2e presents a three-dimensional view of the fault filled with G_C values. Here, one can observe how G_C values change depending on the geometry of the San Ramón fault. As expected, higher G_C values are associated with the most significant geometric irregularities, and they can be regarded as geometric barriers to rupture propagation.

Regarding stress states, some researchers acknowledge that the highest concentrations of potential energy stored in faults may be strongly associated with stress gradients (Zaccagnino and Doglioni, 2022). This accumulation of high energy values could also be associated with the presence of fault roughness (e.g. Venegas-Aravena and Cordaro, 2023). This can be seen schematically in Fig. 3a, where angle α_1 creates a higher concentration of shear stresses (red zones) compared to that generated by angle α_0, which is lower (orange zones). This suggests that stress concentrations may be more closely linked to the geometry of contacts than to the materials' composition itself (Pan and Amadei, 1995). This can be summarized in the relationship between normal stress σ, shear stress τ, and the angle of roughness α as described by (Barton and Choubey, 1977):

$$\tau \approx \sigma tan(\phi_B) \tag{3}$$

where $\phi_B = \phi_A + \theta$ and ϕ_A corresponding to the angle of friction. In this regard, the maximum strength will increase depending on the existing roughness, so rougher areas will tend to store more shear stresses. Eq. (3) is depicted in the black curve in Fig. 3b, where the gray rectangle corresponds to the case where the roughness angle increases for a ϕ_A equal to 30 degrees.

Given the direct relationship between shear stresses and normal stresses, the dependence of the total elastic energy density u_e on sigma can be expressed as follows (Lifshitz et al., 1986; Dove, 2003):

$$u_e \propto \sigma^2 \tag{4}$$

It is important to note that the available energy can be associated with the pre-rupture stress states (Venegas-Aravena et al., 2024) rather than with stress drops. This is exploited by the Heterogeneous Energy-Based method to prescribe the available energy (Venegas-Aravena, 2023b). If we also consider that the distribution of elastic energy density consists of small angles, the dependence of shear stress on the angles representing the geometric irregularities of the fault can be written as: $\sigma \sim 1/\alpha$. This means that the dependencies of fracture and elastic energies on the roughness angle are different.

According to Venegas-Aravena (2023), the available energy ΔW_0, can be interpreted as the product of a function representing the stress state S_0, and a coupling function C. In this case, the stress states correspond to the distribution given by Eq. (4), while the distribution C is associated with the aspect ratios of the sides of the rupture area if this area is considered approximately as a rectangle, as defined by Leonard (2010). It's important to note that the aspect ratio in the HE-B method is used in the distribution C as a reference, as the rupture area is directly linked to residual energy, which also depends on fracture energy. Therefore, it is expected that the final aspect ratios will deviate from the relationships shown by Leonard (2010).

Table 2. Physical parameters used in the simulations and results.

Variable	Symbol	Value	Units
Strike spacing	dx_F	61.0910	m
Dip spacing	dy_F	93.7622	m
Medium density	ρ	1900	$kg \cdot m^{-3}$
P-wave velocity	v_p	6000	$m \cdot s^{-1}$
S-wave velocity	v_s	3464	$m \cdot s^{-1}$
Shear modulus	μ	3.2×1010	$kg \cdot m^{-1} \cdot s^{-2}$
Reference Fracture energy	G_{C0}	1.3×105	$J \cdot m^{-2}$
Peak residual energy	E_p^{res}	6.4×105	$J \cdot m^{-2}$
North-South spacing	dNS	1.0256	km
East-West spacing	dEW	1.2245	km
Reference length	L_{ref}	20	km
Reference width	W_{ref}	10	km
Average Slip	$\bar{u}$	0.9103	m
Slip asperity	$u_{asp} = 1.5 \times \bar{u}$	~1.35	m
Maximum slip	u_p	3.75	m
Time step	dt	0.0176	s
Ruptured area	A	8x25	km^2
Asperity area	A_{asp}	46 (~23%)	km^2
Seismic moment	M_0	7.2x1018	Nm
Magnitude	M_W	~6.5	Dimensionless

Regarding to the San Ramón faut, the latest estimates suggest that it may only accommodate earthquakes with a magnitude close to 6.5 (Yañez et al., 2020). These correspond to approximate lengths and widths of $L \sim 20$ km and $W \sim 10$ km, respectively, following Leonard (2010) formalism (Table 2). This formalism indicates that both length and width are related by a power law of the form $W \sim L^{2/3}$, while the length is associated with the reference seismic moment $M_{0_{ref}}$, in this case, associated with the magnitude 6.5 found by Yañez et al. (2020) in the form $L \sim M_{0_{ref}}^{2/5}$ (Leonard, 2010; Venegas-Aravena, 2023a). It is worth noting that the values of L and W closely match the fault dimensions. This further supports the correctness of the magnitude estimate obtained by Yañez et al. (2020) for

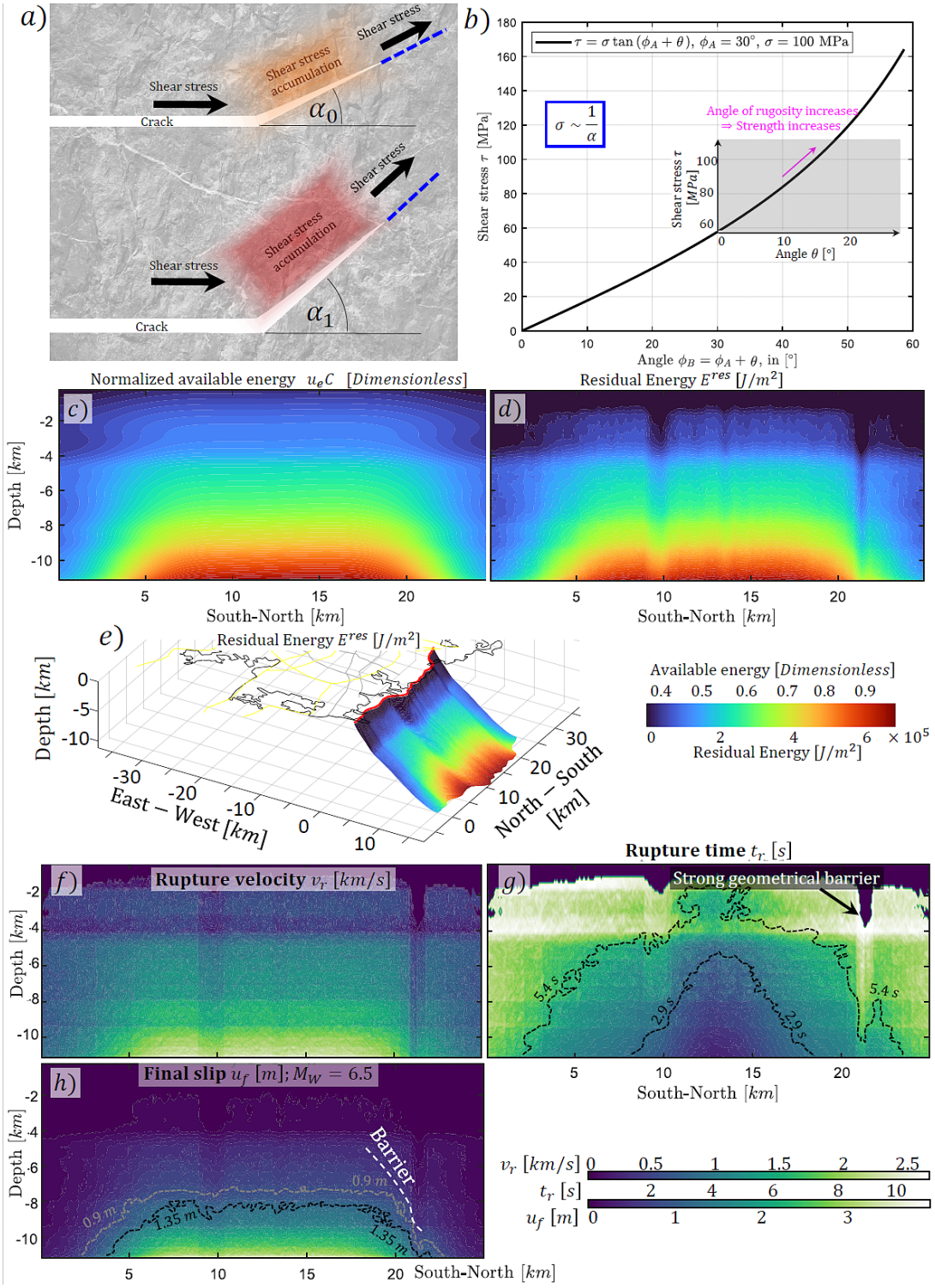

Figure 3. (a) Schematic representation of shear stress concentration as a function of changing roughness angle, or inclination, experienced by a rupture as it propagates through an irregular fault. A greater angle implies higher concentration (depicted in red tones). (b) Increase in shear stress as a function of the friction and roughness angles, ϕ_A and θ respectively. The gray rectangle illustrates how stress increases when considering a higher roughness angle θ for a friction angle ϕ_A equal to 30 degrees. (c) Normalized available energy defined as $u_e C$ when C corresponds to a high-coupling rectangle located at the base of the fault. The non-normalized distribution is obtained by considering a factor, γ. For this study, γ was set to 2 J/m^2. (d) Distribution of residual energy indicating that the rupture does not reach the surface, i.e., $E^{res} = 0$ (dark blue tones). (e) Three-dimensional view of the residual energy. Higher values are concentrated in the deeper sections of the fault. (f), (g), and (h) depict rupture velocity, rupture time, and final slip, respectively.

this fault. This defines an area with sides L and W, where the coupling values inside are 1 and decay exponentially outside of it (Venegas-Aravena, 2023b). Subsequently, the distribution of available energy is $\Delta W_0 \sim u_e C$. A normalized version (Δw_0) is shown in Fig. 3c, with the most coupled zone located in the deeper section of the fault (shades of red). The inverse relationship between normal stress and the angle θ results in low values of available energy in the shallower part of the fault, which is further reinforced when considering a patch of high coupling values in the deeper section of the fault. This region of low available energy in the shallower part is represented by shades of blue in Fig. 3c.

To recover the units of available energy, the normalized version must be multiplied by a factor γ that ensures there are available energy values greater than fracture energy. This means that the residual energy can be written as:

$$E^{res}(x) = \gamma \Delta w_0 - G_C(x) \tag{5}$$

The factor γ will be larger to generate larger earthquakes while maintaining the distribution along the fault. If f is too small, E^{res} could always be negative, preventing any rupture from occurring, while very large values of γ would result in ruptures that would break the entire fault, and the rupture would not be self-arrested. This implies that the parameter γ should be comparable to the values of G_C. For example, Fig. 3d shows the distribution of residual energy when is γ 2 times the maximum value of G_C, as used by Venegas-Aravena (2024). This means that the deeper sections of the fault can have available energies on the order of 11×10^5 J/m^2, while the shallower areas have values of 1×10^5 J/m^2. Since the values of G_C in the shallower part are greater than 4×10^5 J/m^2, E^{res} is negative in the shallow section of the fault, ensuring that the rupture must stop before reaching the surface, thus ensuring it is a self-arrested rupture. Figure 3e depicts a three-dimensional view of the E^{res} distribution in the San Ramón fault.

4. Rupture simulation

In the HE-B method, rupture is assumed to initiate where E^{res} is at its maximum as it is the zone with the highest likelihood of rupture. The HE-B method's focus on this specific zone ensures that the model's rupture initiation is physically realistic. It links the starting point of the earthquake to the location where the fault's properties (high stored energy and low resistance) are most conducive to rupture. This approach also helps the model naturally satisfy the asperity criterion, as the rupture begins in a high-energy zone and propagates to less energetic areas (fostering the self-arrested stage). Additionally, E^{res} determines the rupture parameters of final slip and rupture velocity as $u_f = E^{res} \times G_C \times v_r$ and $v_r = a_0 + b_0 \times E^{res} + c_0 \times \nabla E^{res}$. This means that are determined by establishing direct spatial correlations with the residual energy. This approach is based on a physical principle: areas with less residual energy have less capacity to sustain a large slip or high-speed rupture propagation (Venegas-Aravena, 2023b). Subsequently, the rupture time is defined as $t_r = d_0 + e_0 \times t(r) + f_0 \times \int (1/v_r) dr$, where a_0, b_0, c_0, d_0, e_0 and f_0 are constants defined in Venegas-Aravena (2023b) and $t(r)$ is the rupture time for a homogeneous elliptical rupture.

The distributions of rupture velocity, rupture time, and final slip are depicted in Fig. 3f, 3g, and 3h, respectively. It can be observed that the values of v_r decrease from 2.6 km/s to 0.1 km/s towards the shallow edges of the fault. Darker regions in Fig. 3f indicate the imprint left by high G_C values (black arrow) implying reduced rupture velocities. Rupture time, as shown in Fig. 3g, indicates that rupture initiates near the midpoint of the fault in its deepest part (dark blue tones). Figure 3h displays the final slip values, revealing that higher u_f values are found in the deepest region, decreasing towards the shallower area, akin to the E^{res} distribution. The average slip $\bar{u}$ is approximately 0.9 m, with the rupture area measuring approximately 8×25 km^2, resulting in an earthquake of an estimated magnitude of 6.5 (Table 2). The region with values greater than 1.5 times the average slip, considered as asperities (Somerville et al., 1999), encompasses about 23% of the rupture area (Table 2).

The evolution of the rupture can be divided into three distinct stages. The first stage occurs when the rupture front begins to propagate from the deepest part towards the shallower section of the fault, as depicted by the white arrow in Fig. 4a, representing the onset of the rupture through slip rate. The second stage corresponds to the bilateral advancement of the rupture, as illustrated by the white arrows in Fig. 4b and 4c. In Fig. 4d, a three-dimensional view of the rupture at the moment shown in Fig. 4c is presented, with bilateralism indicated by magenta arrows.

It is important to note that the area on the surface enclosed by the segmented blue curves represents the projection of the bilateral rupture direction (magenta arrow pointing south).

The final stage corresponds to the arrest stage, as shown in Fig. 4e, 4f, 4g, and 4h, which begins when the northern rupture front encounters the barrier indicated by the segmented yellow curves in Fig. 4e, 4f, and 4g. A video depicting the evolution of the rupture can be found at the following link: https://youtu.be/R_DfrPL0Wps.

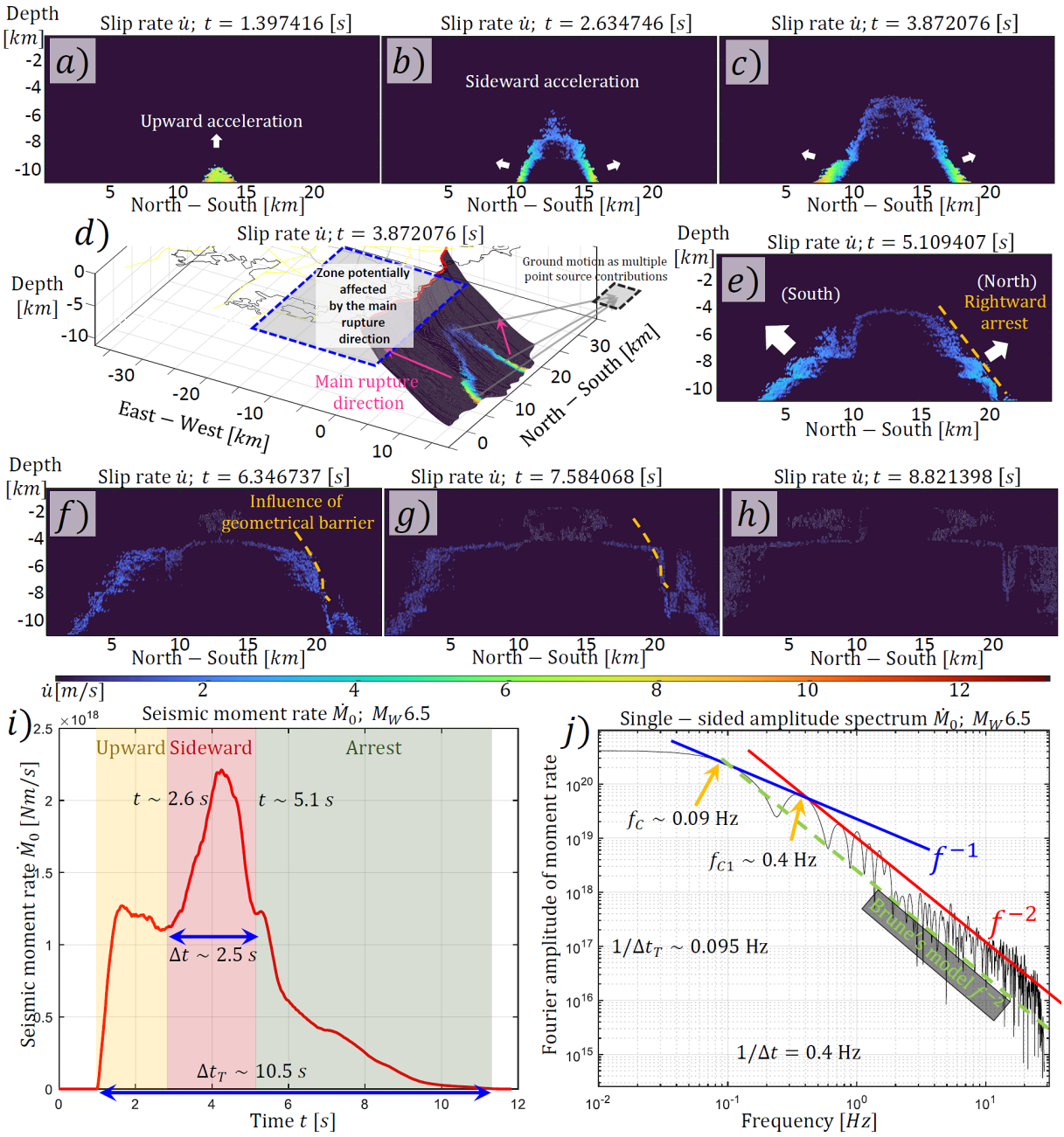

Figure 4. (a), (b), and (c) depict the initial seconds of the rupture through the slip rate (shades from light blue to red). Initially, it heads towards the shallower area (white arrow in (a)) before becoming bilateral (white arrows in (b) and (c)). (d) shows the three-dimensional view of the bilateral advancement of the rupture observed in (c) (magenta arrows). The area marked on the surface enclosed by the segmented blue curve represents the surface projection (south) of the bilateral advancement of the rupture front. (e), (f), and (g) illustrate how the northern section stops faster than the southern section due to the presence of a barrier (yellow segmented line). (h) indicates when the entire rupture front starts to halt. The moment magnitude rate is shown in (i), while its spectrum is presented in (j). The areas of colors yellow, red and green in (i) represents the stages of the ruptures (upward, sideward and arrest respectively).

This evolution of the rupture is summarized in the seismic moment rate evolution shown in Fig. 4i. In this figure, a sudden increase in $\dot{M}_0$ at around 1 second is observed, marking the stage when the rupture starts propagating from the deepest part towards the shallower section of the fault (yellow area). The bilateral stage is characterized by a burst in the seismic moment rate beginning at around 2.6 seconds and lasting for approximately 2.5 seconds (red area in Fig. 4i). The arrest stage commences around 5.1 seconds and is characterized by a gradual decrease in the seismic moment rate, as indicated in the green area of Fig. 4i. Thus, the total duration of the earthquake is approximately 10.5 seconds. As for the $\dot{M}_0$ spectrum, it is characterized by a double corner frequency with decay rates of f^{-1} and f^{-2} (Fig. 4j). The first decay occurs between frequencies of 0.09 Hz and 0.4 Hz, while the f^{-2} decay occurs for frequencies greater than 0.4 Hz. It is important to note that the first corner frequency is equivalent to the inverse of the rupture time (1/10.5 Hz), while the second one is associated with the time it takes to break the seismic moment burst. This corresponds to the time highlighted in the red area in Fig. 4i (1/2.5 Hz).

5. Ground motion simulation

While subsurface heterogeneity undoubtedly influences seismic wave propagation, the modeling of a homogeneous medium offers a relevant initial approximation, particularly when coupled with energy-constrained, heterogeneous rupture simulations (as presented in Section 3). This simplification significantly reduces the computational burden, allowing for a focused analysis on rupture dynamics and surface wave amplification, both of which are critical aspects of seismic hazard assessment. Furthermore, the application of energy constraints within the rupture simulation partially compensates for the simplified propagation medium, as energy distribution directly impacts wave generation. Therefore, although a heterogeneous model would provide greater detail, the combination of energy-constrained, heterogeneous rupture with homogeneous medium propagation presents a pragmatic balance between accuracy and computational efficiency, enabling the derivation of meaningful results for seismic hazard evaluation. Then, the ground motion at each point in the city of Santiago, when considering the fault's geometry shown in Fig. 4d, can be calculated using the displacement field equations as shown by Aki and Richards (1980). This field accounts for near, intermediate, and far-field displacement. These fields exhibit different geometric attenuations. For instance, the near-field, intermediate-field, and far-field exhibit attenuations on the order of r^{-4}, r^{-2}, and r^{-1}, respectively. The intermediate and far fields are directly proportional to the seismic moment M_0 and seismic moment rate $\dot{M}_0$, respectively, while the near field is proportional to the time integral of the seismic moment. This allows for the calculation of the displacement field in various directions from the seismic source. In this heterogeneous scenario, the displacement field at a point on the Earth's surface is determined by the contribution of each sub fault, each having different values for rupture parameters such as slip rate, as well as varying locations and orientations within the fault, as presented in Venegas-Aravena (2023a) and Venegas-Aravena (2024). This means that each point on the surface receives contributions from different sub faults breaking at various distances.

In this case, the medium is homogeneous with a density of $\rho = 1900$ kg/m^3 and a shear modulus $\mu = 3.2 \times 10^{10}$ kg/ms^2, while the S-wave and P-wave velocities are 3464 m/s and 6000 m/s, respectively (Table 2). The spacing on the Earth's surface is 1.0256 km in the north-south direction and 1.2245 km in the east-west direction (Table 2). The area under consideration measures 40 km in the north-south direction and 60 km in the east-west direction, effectively covering the entire city of Santiago. The velocity field within this area is depicted in Fig. 5. This figure depicts the velocity field at different time intervals, while a video illustrating this evolution can be found at the following link: https://youtu.be/R_DfrPL0Wps.

This velocity field is used to characterize the ground motion intensity at different locations. For instance, it can be observed that the maximum velocity values are on the order of several tens of centimeters per second, with a peak-to-peak value close to 35 cm/s. This is illustrated in Fig. 6a, where the easternmost region, as well as areas near the San Ramón fault (red curve), exhibit peak ground velocity (PGV) values exceeding 30 cm/s (depicted in yellow tones in Fig. 6a). The urban area, marked by the black curve, experiences PGV values surpassing 10 cm/s. The area enclosed by the segmented black lines roughly outlines the central and eastern part of the city, where PGV values exceed 20 cm/s on average.

Another measure of ground motion intensity at a specific location is described by the maximum acceleration experienced at a particular site during an earthquake, which is referred to as Peak Ground Acceleration (PGA). It is typically expressed as a fraction of the Earth's gravitational acceleration (g). In this case, the area closest to the

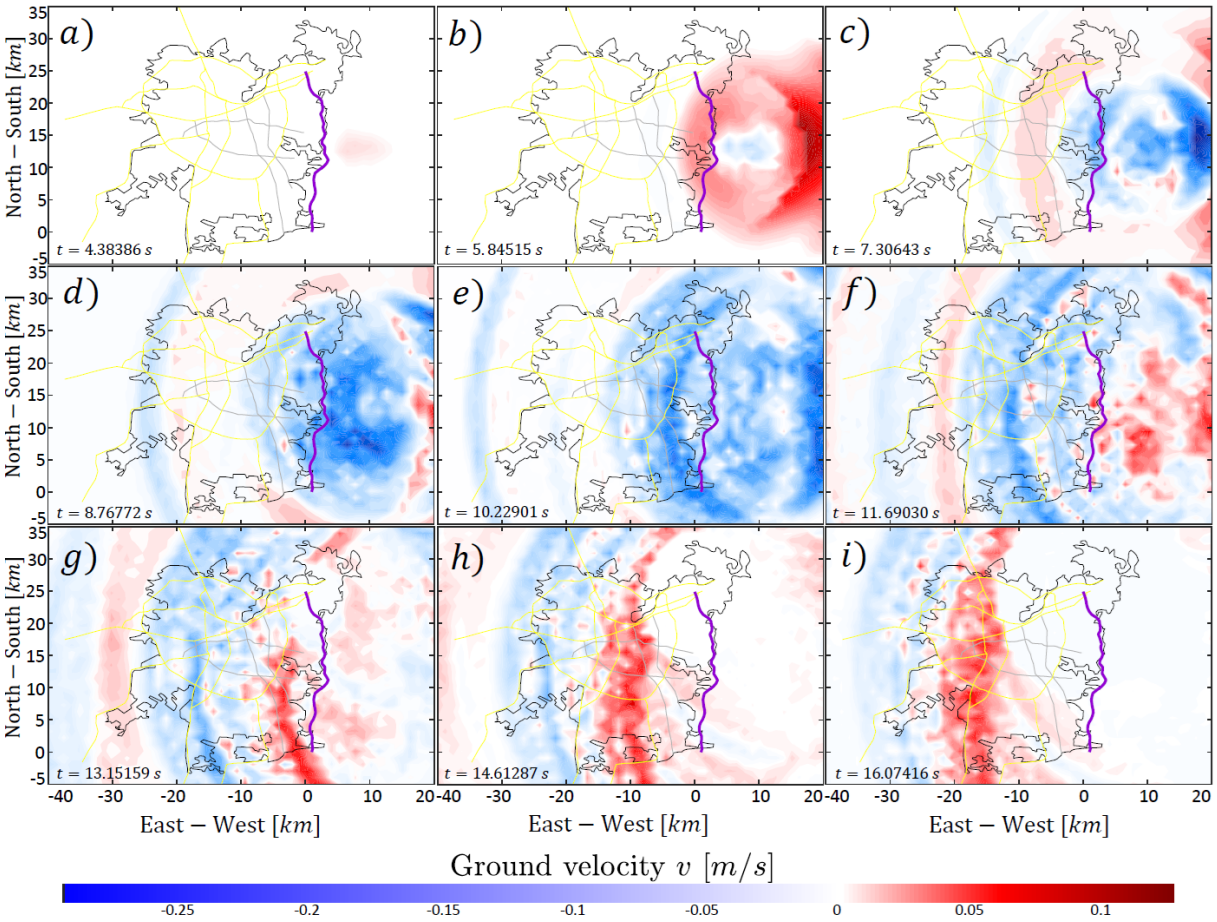

Figure 5. Ground motion evolution using the velocity displacement at 9 different time instants.

fault (eastern Santiago) may experience PGA values exceeding 0.6 g. This is represented by the orange to red tones within the region enclosed by the segmented red curve in Fig. 6b. Here is important to note that this calculation does not consider site effects. The attenuation of acceleration with respect to the distance from the fault is depicted by the gray curves in Fig. 6c. The average attenuation value is shown by the segmented blue curve, while the red curve represents the reference value provided by Kanno et al. (2006). In the first 6 km, the obtained average PGA values (segmented blue curve) are lower than those indicated by the red curve. However, this trend reverses at greater distances (up to approximately 30 km from the fault). This is relevant as the city of Santiago is mostly located within 30 km of the fault. This suggests that areas even as far as 25 km from the fault could experience ground accelerations close to 0.2 g, with peaks potentially reaching around 0.65g. In other words, significant variability may exist. Figure 6c also suggests that eastern Santiago (highlighted at a 13 km distance, as shown in the insect of Fig. 6b and the red square in Fig. 6c), may experience an average PGA exceeding 0.4 g.

The color scale in Fig. 6d shows that the highest PGA values, exceeding 0.6g, are concentrated in the eastern sector, particularly within the red box. This zone directly overlies the San Ramón Fault (red curve) and is characterized by a strong sediment effect, which amplifies ground shaking. Similar to the PGA map with sediment effects, Fig. 6e indicates that the highest PGV values (up to 0.6 m/s) are located in the eastern part of the city (orange to yellow shades), closely mirroring the patterns of PGA. This suggests that the ground shaking in these eastern zones could be extremely strong. In contrast, the western part of the city, marked with blue and purple (Fig. 6d), shows much lower PGA values, generally below 0.3g. This clear difference highlights the critical role of both fault proximity and sediment amplification in determining the seismic risk in Santiago.

Figure 7 provides more detailed information on how ground acceleration changes over time through the seismograms of critical infrastructure locations listed in Table 1. These seismograms depict significant ground motion, with PGA values exceeding 0.4 g at a distance of 18 km from the fault. The red lines indicate the arrival of P and S waves at each location. These lines diverge as the different wave velocities become more pronounced with

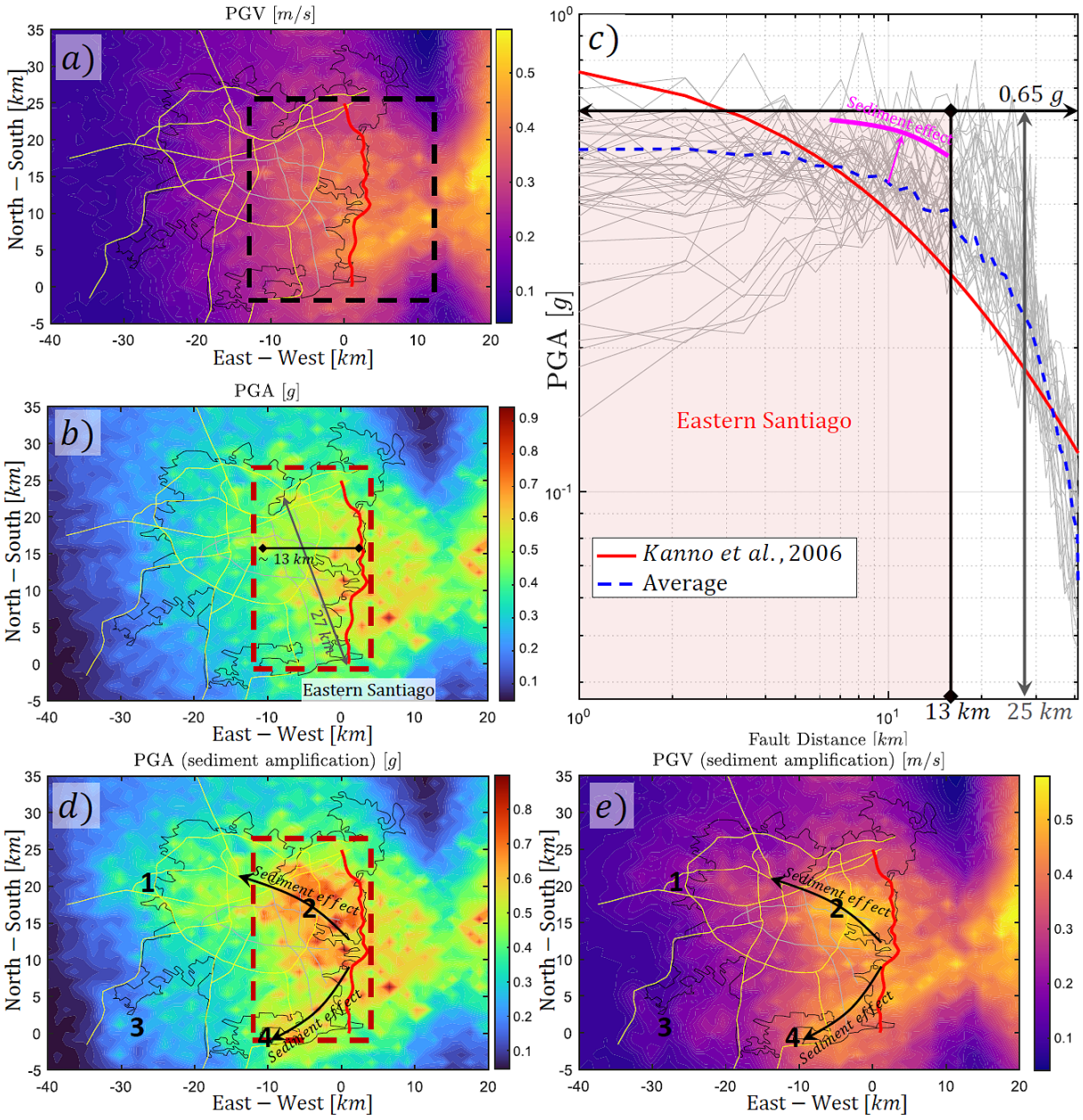

Figure 6. A map indicating maximum ground velocity speeds. Within the city, these are concentrated near the San Ramón Fault (orange and yellow shades), with values close to 0.25 m/s. A map of maximum ground accelerations in units of g. Values exceeding 0.4 g can be found up to approximately 15 km from the fault (green to red shades). Ground motion attenuation as a function of distance (gray curves) alongside the average (dashed blue curve) and the model by Kanno et al., 2006 (red curve). The red area represents the East-West distance marked in (b), which corresponds to the eastern half of Santiago and can reach values of up to 0.65 g.

distance. It's worth noting that locations closest to the epicenter within Santiago, particularly in the eastern sector, exhibit exceptionally high PGAs, surpassing 0.6 g. For instance, the highest recorded value corresponds to the site of the La Reina nuclear reactor, marked with a yellow triangle, registering a PGA of 0.6754 g. Additionally, hospitals labeled as H3, H4, and H5 also display elevated PGAs, specifically 0.6612 g, 0.6453 g, and 0.6356 g, respectively (Table 1 and Fig. 7). The other hospitals (H1 and H2) also report PGAs exceeding 0.5 g. The government center LM exhibits a PGA of approximately 0.41 g, while the educational center SJ approaches a 0.5 g PGA (Table 1 and Fig. 7). Furthermore, Table 1 indicates that the PGV values at these locations all exceed 20 cm/s.

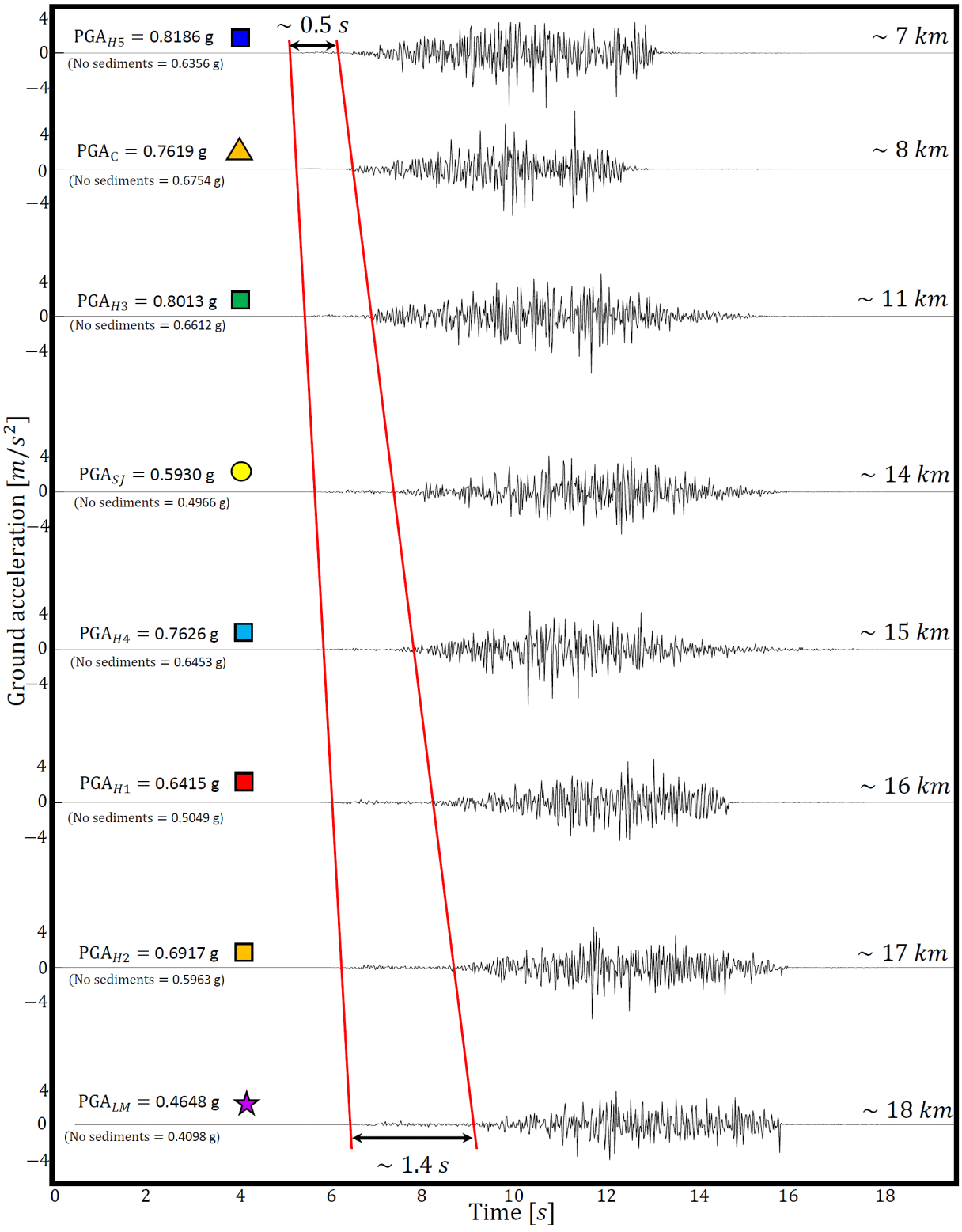

Figure 7. Accelerograms obtained at the locations corresponding to the critical points described in Table 1 and Fig. 1b and 1c. The red lines approximately indicate the arrival of the P and S waves at each point.

6. Summary and discussions

Chile consistently faces seismic risks due to recurrent subduction earthquakes affecting the Chilean margin, which can result in peak ground accelerations (PGA) on the order of 1 g near coastal areas (Maringue et al., 2022). Despite this, the seismic risk and threat to cities like Santiago are not factored into urban planning policies due to limited information about fault seismicity (e.g. Rivera et al., 2020). Therefore, seismic risk analyses based on hypothetical rupture scenarios are essential to estimate vulnerability within urban areas such as Santiago, primarily due to the strong ground motion generated by nearby faults (e.g. Hussain et al., 2020).

Unlike the megathrust earthquakes common in Chile, which occur far off the coast due to subduction, the San Ramón Fault is particularly significant for seismic risk assessment in Santiago because it is a shallow, reverse crustal fault of 25km length that is located directly beneath the eastern section of the city. With approximately 40% of its total length already urbanized, and projected to reach 75% in the future, its proximity to critical infrastructure, including hospitals and government centers, makes it a critical threat to this highly populated urban center. Furthermore, the soft soil sediment conditions in Santiago's basin could amplify ground motion, increasing the potential for widespread damage even from moderate magnitude events. In other words, this proximity and soil type means that an earthquake would generate significantly higher shaking intensities than a distant event of similar magnitude.

Prior studies have suggested that this fault has the potential to generate earthquakes with magnitudes close to M_w 7 and, consequently, the potential for devastation (Armijo et al., 2010; Riesner et al., 2017). For example, the projected damage from this fault to nearby areas is roughly ten times higher than that from a subduction earthquake along the Chilean coast. This is due to its peak ground acceleration (PGA) values, which can reach around 0.6 g within a few kilometers of the fault when dealing with earthquakes of magnitude M_w 7.5 (Pérez et al., 2014; Estay et al., 2016; Ammirati et al., 2019; Hussain et al., 2020). Nevertheless, analyses of the geological deformation patterns along the fault suggest that the San Ramón Fault's maximum magnitude is closer to M_w 6.5 (Estay et al., 2016; Yañez et al., 2020). Therefore, seismic hazard and risk analyses for this fault should take into account hypothetical rupture scenarios of this magnitude. Hence, this study addressed a case of heterogeneous rupture conditions using the HE-B method (Venegas-Aravena, 2023).

It is crucial to emphasize that the HE-B method represents a paradigm shift from probabilistic and epistemic analyses, as it is predicated on the quantification of energy available within a fault. This approach is substantiated by the observed high spatial correlation between accumulated energy and the final slip distribution, as evidenced in large earthquakes through inter-seismic coupling analyses and dynamic rupture simulations under heterogeneous conditions (e.g. Moreno et al., 2010; Venegas-Aravena et al., 2024). Furthermore, fracture energy admits various experimentally validated interpretations, including material property, earthquake size scaling, energy dissipation modality, and fault roughness proportionality. In this study, the latter perspective is adopted, rendering initial fracture energy values merely referential, with the emphasis placed on the fault's geometric variability, which is derived from field studies (Section 2). Consequently, the rupture process variability is entirely constrained by fault energy, positioning this analysis as a hypothetical rupture scenario directly informed by the fault's energetic conditions. This energy-based physical paradigm imposes methodological constraints, as it restricts the analysis to a singular scenario. In this study, this scenario represents the maximum rupture case dictated by the available energy storage capacity of the fault.

By incorporating the geometry of the San Ramón Fault, which is directly related to fracture energy G_C, as shown in Eq. (2). Specifically, Fig. 2c and 2d illustrate that these geometric irregularities create frictional barriers within the HE-B method. This implies that the rupture requires a significant amount of energy to overcome the high G_C values present in the shallow part of the fault. This characteristic imposes that the most likely rupture scenario in the San Ramón Fault is one in which the residual energy is lower in the shallow portion of the fault, as depicted in Fig. 3d and 3e. Due to the limited resolution regarding subsurface heterogeneities within the city of Santiago, the decision was made to utilize readily available data, such as ground motion amplification. While this approach is not ideal, the integration of a well-defined heterogeneous source with a high-resolution surface amplification distribution can serve as an approximation for ground motion. Nevertheless, it is imperative to suggest that future analyses should explore the incorporation of subsurface heterogeneities to achieve more precise results.

Under these conditions, a simulated M_w 6.5 earthquake scenario showed significant ground motion variations comparable to those previously suggested for an M_w 7.5 earthquake. This indicates that past PGA measurements were underestimated, as values of 0.6 g can be reached with smaller M_w 6.5 earthquakes when considering fault

heterogeneities and geometry. This is most evident in the ground motion attenuation curve as a function of distance from the fault (Fig. 6c). Specifically, Fig. 6c shows a deviation from the PGA values proposed by Kanno et al., 2006 (red curve). This means that areas closer to the fault (~1 km) tend to have a PGA less than 0.7 g. However, the PGA values obtained at these distances range from 0.15 g to 0.7 g, indicating significant variability in ground motion (gray curves). Another range where the results deviate from the Kanno et al. (2006) model is between 10 km and 30 km, which is where much of the city of Santiago is located. In particular, it is shown that almost the entire city can experience PGAs greater than 0.3 g (light blue tones in Fig. 6b), even reaching values exceeding 0.5 g at around 20 km from the fault (green tones in Fig. 6b). Some PGAs near 0.65 g can also be observed up to distances of around 20 km in lesser extent (Fig. 6c). These high PGA values at 20 km are even higher than those found in simulations of earthquakes of the same magnitude when considering flat faults (Ojeda et al., 2021). In this regard, the increase in PGA can be associated with the effect of heterogeneous rupture on a non-planar fault. This implies that ground motion at a point on the surface corresponds to the superposition of different locations on the fault that move by different amounts, as well as different angles of incidence. In terms of the average value (blue dashed curve in Fig. 6c), PGA values reach 0.4 g at 10 km from the fault. This value is approximately 3.9 m/s^2, which is quite close to the PGA value found in recent stochastic simulations and real earthquakes with magnitudes around 6.5 (e.g. Ji and Archuleta, 2021). Here it is important to emphasize that the ground motion did not account for the effect of surface waves or site effects, so ground accelerations could potentially be even higher.

Particular attention should be given to the eastern region of Santiago, as the accelerations found there are generally above 0.4 g, as indicated by the area outlined by red dashed lines in Fig. 6b. Additionally, large areas have values exceeding 0.65 g, with some even exceeding 0.8 g. It's important to note that these locations only recorded accelerations on the order of 0.2 g during the 2010 Maule earthquake (Mw8.8) (Barrientos, 2010; Saragoni et al., 2010), and only cities close to the Maule 2010 event, such as Concepción, recorded comparable accelerations (>0.6 g) to those expected in the eastern zone of Santiago (Saragoni et al., 2010). This analysis is significant since a considerable portion of the urban area could experience accelerations exceeding 0.3 g. When considering the western section of the city, it's important to note that this area has lower-density sediments compared to the eastern zone (Yañez et al., 2015). This means that the western sector could experience ground motion amplification. This was observed during the 2010 Maule earthquake, where eastern stations recorded PGAs close to 0.3 g (Peñalolen), while the western sector had PGAs close to 0.5 g (Maipu) (Saragoni et al., 2010). That is, the western sector of the city experienced PGAs approximately 1.6 times those measured in the eastern sector. In this regard, it could be expected that site effects in the western zone of Santiago might lead to a similar difference in PGA for this earthquake. In other words, if the eastern zone may record PGAs close to 0.7 g for this hypothetical rupture, the presence of sedimentation could potentially generate PGAs exceeding 1 g in the western sector. However, further studies are required to determine if this logic can also be applied to an earthquake on the San Ramon Fault. Nevertheless, this implies that the expected damage from an earthquake on the San Ramón Fault could surpass that of the 2010 Maule earthquake (M_w 8.8) in the City of Santiago. This is noteworthy because some authors have found that damage due to ground motion can begin with values equal to or less than 0.1 g (Bolt and Abrahamson, 2003). Concepción, a city close to the 2010 Maule earthquake, experienced significant damage, with PGAs around 0.6 g, resulting in building collapses and structural damage (Rojas et al., 2011; Youssef et al., 2011; Song et al., 2012; Deger and Wallace, 2015). Therefore, it is expected that the entire city of Santiago could suffer severe damage in the event of an earthquake with characteristics similar to those presented in this study.

Another important aspect of ground motion is the differentiation between the hanging wall and the footwall. Specifically, the eastern side of the fault (hanging wall), where the Andes Mountain range is located, exhibits higher PGA values at greater distances compared to the western side of the fault, as shown by the red shades in Fig. 6b. This could be associated with observations suggesting more damage and ground motion in the hanging wall than the footwall for reverse faults (e.g. Pathier et al., 2006). Fortunately, there is almost no population in that area. However, mass removal processes would be expected in the mountainous front, as occurred in the case of the 2010 Maule earthquake (e.g. Mardones and Rojas, 2012). This is of particular importance because these mountainous areas are the sources of freshwater that supply the city of Santiago and it could be affected by the debris (Ahumada et al., 2012).

The utilization of fault sources modeled as point sources with analytically defined equations within a non-discretized medium, where the temporal variation at each surface point corresponds to the superposition of these analytical waves, precludes the occurrence of spatial aliasing. Given a sampling frequency on the order of 60 Hz, temporal aliasing is expected to manifest at frequencies exceedingly approximately 30 Hz. Notwithstanding this, not all

frequencies undergo attenuation to the same extent. For instance, the attenuation of a seismic wave's amplitude as a function of frequency over a travel distance (x) can be described by the following relationship (e.g. Aki and Richards, 1980):

$$A(x) = A_0 e^{-\frac{\pi f x}{QV}} \tag{6}$$

Where $A(x)$ represents the wave attenuation at a distance x, A_0 is the initial wave amplitude (proximal to the source), f denotes the wave frequency, Q is the quality factor of the medium (for sandstone, Q can range from 50 to 200 (Pandit and King, 1979), thus a value of $Q = 100$ will be adopted), and V is the wave velocity in the medium (distinct for P-waves and S-waves). Here, it is assumed that acceleration is proportional to the wave amplitude; consequently, A_0 represents the maximum acceleration, as depicted in Fig. 6d, which is approximately 0.9 g. With this, the attenuation of the frequency associated with both the P-wave and the S-wave can be calculated. This is illustrated in Fig. 8a, b, c, and d for distances of 5, 10, 20, and 30 km, respectively, where the red curves indicate the attenuation for P-waves and the blue curves for S-waves. The transparent green rectangle shows the approximate ground acceleration for these distances according to Fig. 6d, which ranges between 0.7-0.8 g, 0.5-0.6 g, 0.4-0.6 g, and 0.3-0.45 g for fault distances of 5, 10, 20, and 30 km, respectively. This transparent green

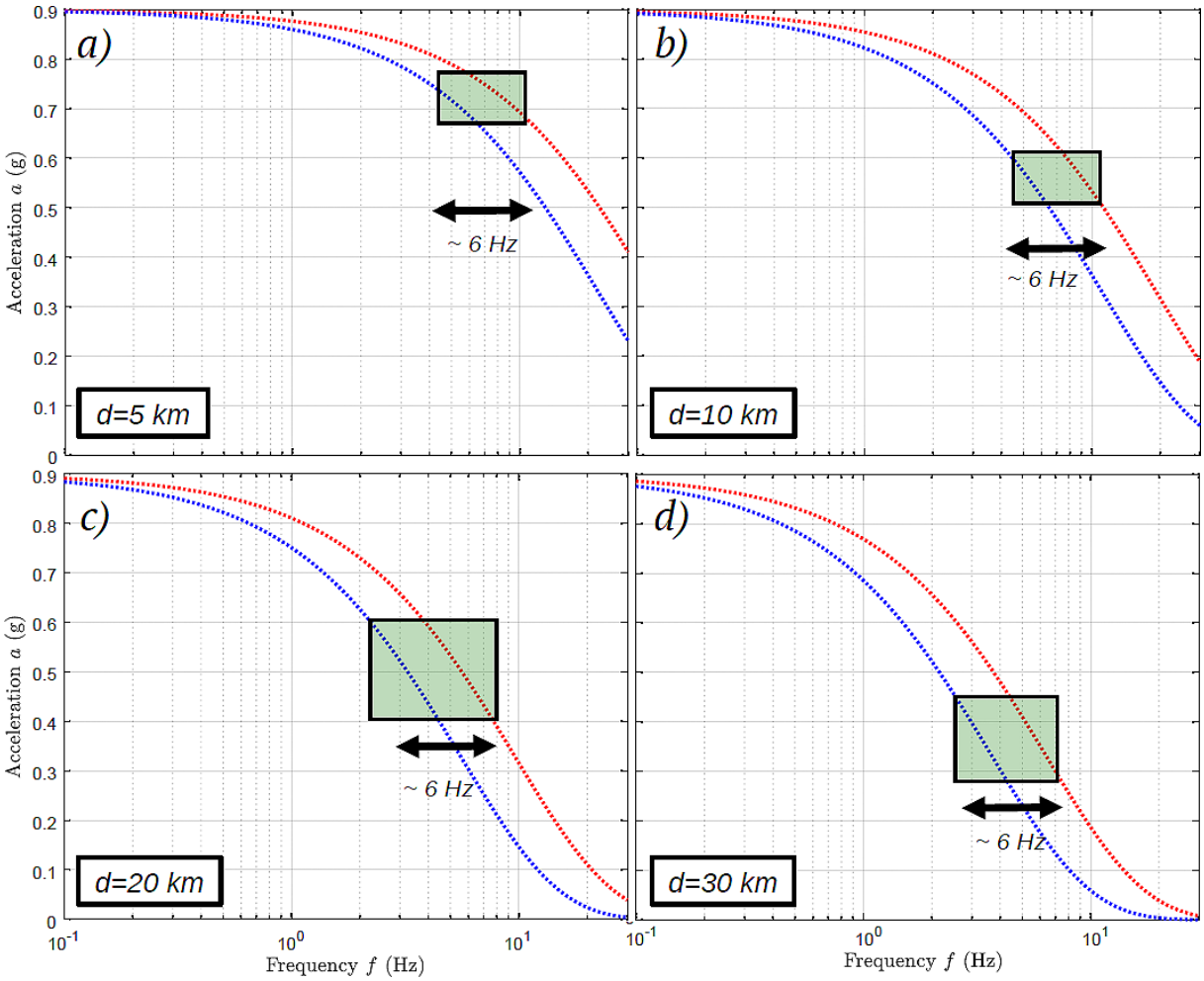

Figure 8. The decay of ground acceleration with increasing source distance is illustrated at 5 km (a), 10 km (b), 20 km (c), and 30 km (d), as determined by Eq. (6). The red curve represents the P-wave, while the blue curve depicts the S-wave. The green rectangle indicates the approximate accelerations at these respective distances. The attenuation model consistently suggests that these accelerations occur at a frequency on the order of 5-6 Hz, which is lower than the maximum frequency of 30 Hz.

rectangle indicates that the obtained accelerations correspond to maximum frequencies on the order of 6 Hz, which is one-fifth of the maximum sampling frequency (30 Hz).

This suggests that lower frequencies (below 4 Hz) did not generate that level of acceleration at those distances, while higher frequencies (above 8 Hz) were significantly attenuated by the medium. Therefore, the spectral analysis indicates that the maximum accelerations are dominated by a specific frequency range (4-7 Hz) that propagated with less attenuation within that range.

A portion of these peak accelerations may be attributed to the directivity effect associated with the acceleration of the rupture front, analogous to a Doppler effect. For instance, Venegas-Aravena (2023a) demonstrated that as a rupture accelerates in a given direction, the frequency content increases in regions situated ahead of that acceleration direction. Consequently, given the heterogeneous nature of the fault and its variable rupture velocity, it is anticipated that this directivity effect would also contribute to the observed increase in ground accelerations.

With regard to recurrence time, it has been estimated that the San Ramón Fault has an activity rate on the order of 0.5 mm/yr (Armijo et al., 2010), suggesting an M_w 7.5 earthquake approximately every 8000 years (Vargas et al., 2014). However, the scenario presented in this study considered an M_w 6.5 earthquake, which has a recurrence interval of around 1500 to 2000 years (Gürsoy et al., 2007). Therefore, the scenario depicted in this work not only results in higher ground motion due to fault geometry and heterogeneities but also represents a more frequent event than typically anticipated. Unfortunately, there is no information regarding when an earthquake with the characteristics studied here might occur. However, the ground accelerations presented in this study can be considered for future seismic hazard assessments for the city of Santiago, especially concerning critical infrastructure.

In that sense, the areas marked in Table 1 and Fig. 1b which represent critical infrastructure within the city, would be significantly impacted by the strong ground motion. The most critical case is the La Reina nuclear research center (yellow triangle in Fig. 1b and 1c), where the PGA values are close to 0.7 g (Table 1). For reference, it's important to note that the Fukushima-Daiichi reactor recorded PGAs on the order of 0.5 g (~500 Gal) during the Tohoku MW9.0 earthquake in 2011 (https://www.world-nuclear-news.org/RS_Fukushima_faced_14-metre_tsunami_2303113.html). Therefore, the expected accelerations for the La Reina reactor exceed those recorded for the Fukushima-Daiichi Reactor. Additionally, other critical infrastructure such as hospitals would be similarly affected since all of those considered have PGAs greater than 0.5 g (Table 1). This implies that a substantial investment in mitigating the effects of ground motion would be necessary for these locations. These acceleration values highlight the need for future research associated with seismic risk in the area.

7. Conclusions

The main conclusions of this study relate to the ability to use computational models for estimating strong ground motion as a basis for future seismic risk analysis in the city of Santiago, Chile. In this regard, the incorporation of the San Ramón Fault's geometry along with heterogeneous rupture conditions is crucial for generating higher ground accelerations. Based on the findings, it can be concluded that:

- Considering the San Ramón Fault's geometry suggests that potential ruptures are strongly constrained in depth. This means that a significant amount of energy is required to bring the rupture to the surface, favoring deeper ruptures. Therefore, hypothetical rupture scenarios should consider nucleation to be located in the deeper section of the fault, arresting before the rupture front reaches the surface.
- Heterogeneities in the rupture process generate stronger ground motion than previously estimated. In general, the ground motion is more intense than what the city experienced during the 2010 Maule earthquake, but with a shorter duration (approximately 12 seconds).
- The obtained strong ground motion suggests that the eastern sector of Santiago may produce peak ground accelerations (PGAs) greater than 0.6 g. Additionally, past earthquake-induced site effects suggest that the western sector may generate PGAs close to or exceeding 1 g. Therefore, this scenario indicates that severe damage would be expected in many structures, including the collapse of various buildings throughout the city.
- An earthquake of these characteristics could occur in a shorter time frame, approximately every 1,500 to 2,000 years.
- Critical infrastructure, such as the nuclear reactor, water sources and hospitals, would be significantly affected. It is necessary to develop seismic hazard mitigation plans for these locations.
- Future analysis should be oriented in the risk associated with the results shown in this work.

Data availability statement. The data and codes used in this work are available at the following reference:
Venegas-Aravena, P. (2023). Strong-ground motion for the city of Santiago (Chile) by using the Heterogeneous Energy-Based method, Data set, Zenodo, doi:10.5281/zenodo.10050539.
Venegas-Aravena, P. (2024). Ground motion amplification of the Santiago basin, Data set, Zenodo, doi.org/10.5281/zenodo.10835822.
Additionally, a video of the rupture and its effect on strong ground motion can be found at this YouTube link: https://youtu.be/R_DfrPL0Wps?si=7z8InDPwAZb5wrvb. For any questions or inquiries, please do not hesitate to contact the author.

Acknowledgements. P.V.-A. acknowledge the anonymous reviewer and the Editor Dr. Licia Faenza for their comments that allowed me to improve the present work. In addition, P.V.-A. also acknowledge the continuous academic and scientific support of the Pontificia Universidad Católica de Chile. Finally, extending the acknowledge to P. Aravena, A. Franklin Venegas for their continuous support.

References

Aki, K. and P. Richards (1980). Quantitative seismology, W. H. Freeman, New York, 742, ISSN:0827-5483.

Ammirati, J. B., G. Vargas, S. Rebolledo, R. Abrahami et al. (2019). The Crustal Seismicity of the Western Andean Thrust (Central Chile, 33°-34° S): Implications for Regional Tectonics and Seismic Hazard in the Santiago Area, B. Seismol. Soc. Am., 109, 5, 1985-1999, doi:10.1785/0120190082.

Aochi, H. and S. Ide (2014). Ground motions characterized by a multi-scale heterogeneous earthquake model, Earth Planets Space, 66, 42, 1-12, doi:10.1186/1880-5981-66-42.

Araya, J., G. P. De Pascale, R. Mardel and S. A. Sepúlveda (2021). The likely Quaternary active El Arrayán fault, Santiago, Chile, Andean Geol., 48, 3, 529-545, doi:10.5027/andgeoV48n3-3256.

Armijo, R., R. Rauld, R. Thiele, G. Vargas et al. (2010). The West Andean Thrust, the San Ramón Fault and the seismic hazard for Santiago, Chile, Tectonics, 29, 2, 1-34, doi:10.1029/2008TC002427.

Barrientos, S. (2010). Terremoto (M=8.8) del 27 de febrero de 2010 en Chile, Rev. Asoc. Geol. Argent., 67, 3, 412-420.

Barton, N. and V. Choubey (1977). The shear strength of rock joints in theory and practice, Rock Mech., 10, 1, 1-54, doi:10.1007/BF01261801.

Bolt, B. A. and N. A. Abrahamson (2003). Estimation of strong seismic ground motions, in Int. Handb. Earthq. Engi. Seismol. L. WHK Kanamori, H. Jennings, P. C. Kisslinger (Eds.), 81, 1B, 983-1001, doi:10.1016/S0074-6142(03)80173-0.

Bommer, J. J., P. J. Stafford, E. Ruigrok, A. Rodriguez-Marek et al. (2022). Ground-motion prediction models for induced earthquakes in the Groningen gas field, the Netherlands, J. Seismol., 26, 1, 1157-1184, doi:10.1007/s10950-022-10120-w.

Booth, E. (2007). The Estimation of Peak Ground-motion Parameters from Spectral Ordinates, J. Earthq. Eng., 11, 1, 13-32, doi:10.1080/13632460601123156.

Bradley, B. A., S. E. Bae, V. Polak, R. L. Lee et al. (2017a). Ground motion simulations of great earthquakes on the Alpine Fault: effect of hypocentre location and comparison with empirical modelling, New Zeal. J. Geol. Geop., 60, 3, 188-198, doi:10.1080/00288306.2017.1297313.

Bradley, B. A., H. N. T. Razafindrakoto and V. Polak (2017b). Ground-Motion Observations from the 14 November 2016 Mw7.8 Kaikoura, New Zealand, Earthquake and Insights from Broadband Simulations, Seismol. Res. Lett., 88, 3, 740-756, doi:10.1785/0220160225.

Brune, J. N. (1970). Tectonic stress and the spectra of seismic shear waves from earthquakes, J. Geophys. Res., 75, 26, 4997-5009, doi:10.1029/JB075i026p04997.

Brune, J. N. (1971). Correction to Tectonic stress and the spectra, of seismic shear waves from earthquakes, J. Geophys. Res., 76, 20, 5002-5002, doi:10.1029/JB076i020p05002.

Candela, T., F. Renard, Y. Klinger, K. Mair et al. (2012). Roughness of fault surfaces over nine decades of length scales, J. Geophys. Res. Sol. Ea., 117, B8, 1-30, doi:10.1029/2011JB009041.

Chen, Y. and H. Yang (2016). Numerical simulation and pattern characterization of nonlinear spatiotemporal dynamics on fractal surfaces for the whole-heart modeling applications, Eur. Phys. J. B, 89, 181, 1-16, doi:10.1140/epjb/e2016-60960-6.

Deger, Z. T. and J. W. Wallace (2015). Collapse Assessment of the Alto Rio Building in the 2010 Chile Earthquake, Earthq. Spectra, 31, 3, 1397-1425, doi:10.1193/060812EQS209M.

De Matteis, G. and M. Zizi (2018). Seismic Damage Prediction of Masonry Churches by a PGA-based Approach, Int. J. Archit. Herit., 13, 7, 1165-1179, doi:10.1080/15583058.2019.1597215.

Dove, M. T. (2003). Structure and Dynamics: An Atomic View of Materials, Mater. Today, 6, 6, 59, doi:10.1016/S1369-7021(03)00639-4.

Estay, N. P., G. Yañez, S. Carretier, E. Lira et al. (2016). Seismic hazard in low slip rate crustal faults, estimating the characteristic event and the most hazardous zone: study case San Ramón Fault, in southern Andes, Nat. Hazard. Earth Sys., 16, 12, 2511-2528, doi:10.5194/nhess-16-2511-2016.

Fang, Z. and E. M. Dunham (2013). Additional shear resistance from fault roughness and stress levels on geometrically complex faults, J. Geophys Res. Sol. Ea., 118, 7, 3642-3654, doi:10.1002/jgrb.50262.

Glehman, J. and M. Tsesarsky (2022). Ground motion variability in Israel from 3-D simulations of M6 and M7 earthquakes, Nat. Hazard Earth Sys., 22, 4, 1451-1467, doi:10.5194/nhess-22-1451-2022.

Graves, R. W. and A. Pitarka (2004). Broadband time history simulation using a hybrid approach, Proc. 13th World Conf. Earthq. Eng., Vancouver, Canada, 1098.

Gürsoy, H., B. L. Mesci, J. D. P. Piper, O. Tatar et al. (2007). The magnetism in tectonically controlled travertine as a palaeoseismological tool: Examples from the Sıcak Çermik geothermal field, central Turkey, in The Geodynamics of the Aegean and Anatolia T. Taymaz, Y. Yilmaz, Y. Dilek (Authors), Geol. Soc. Lond., 291, 1, 291-305, doi:10.1144/SP291.13.

Heping, X. (1989). The fractal effect of irregularity of crack branching on the fracture toughness of brittle materials, Int. J. Fracture, 41, 1, 267-274, doi:10.1007/BF00018858.

Herrera, M. T., J. Crempien and J. Cembrano (2023). Complex Crustal Deformation Controlled by the 3D Geometry of the Chile Subduction Zone, B. Seismol. Soc. Am., 113, 6, 2479-2491, doi:10.1785/0120230062.

Honoré, L., F. Courboulex and A. Souriau (2011). Ground motion simulations of a major historical earthquake (1660) in the French Pyrenees using recent moderate size earthquakes, Geophys. J. Int., 187, 2, 1001-1018, doi:10.1111/j.1365-246X.2011.05193.x.

Hussain, E., J. R. Elliott, V. Silva, M. Vilar Vega et al. (2020). Contrasting seismic risk for Santiago, Chile, from near-field and distant earthquake sources, Nat. Hazard. Earth Sys., 20, 5, 1533-1555, doi:10.5194/nhess-20-1533-2020.

Ji, C. and R. J. Archuleta (2021). Two Empirical Double-Corner-Frequency Source Spectra and Their Physical Implications, B. Seismol. Soc. Am., 111, 2, 737-761, doi:10.1785/0120200238.

Kagawa, T., K. Irikura and P. G. Somerville (2004). Differences in ground motion and fault rupture process between the surface and buried rupture earthquakes, Earth Planets Space, 56, 1, 3-14, doi:10.1186/BF03352486.

Kanno, T., A. Narita, N. Morikawa, H. Fujiwara et al. (2006). A New Attenuation Relation for Strong Ground Motion in Japan Based on Recorded Data, B. Seismol. Soc. Am., 96, 3, 879-897, doi:10.1785/0120050138.

Leonard, M. (2010). Earthquake Fault Scaling: Self-Consistent Relating of Rupture Length, Width, Average Displacement and Moment Release, B. Seismol. Soc. Am., 100, 5A, 1971-1988, doi:10.1785/0120090189.

Li, J., B. Zhou, Z. He, H. Ji et al. (2024). Accessing Near-Field Strong Ground Motions Using a Multi-Scheme Method in the Kalawenguquan Fault, Xinjiang, China, Appl. Sci., 14, 4, 1-20, doi:10.3390/app14041451.

Lifshitz, E. M., A. M. Kosevich and L. P. Pitaevskii (1986). Theory of Elasticity, Third edition, Butterworth-Heinemann, MA, USA, doi:10.1016/C2009-0-25521-8.

Lung, C. W. (1985) Fractals and the fracture of cracked metals (IC-85/123), International Atomic Energy Agency, IAEA-UNESCO, 1-5.

Maldonado, V., M. Contreras and D. Melnick (2021). A comprehensive database of active and potentially-active continental faults in Chile at 1:25,000 scale, Sc. Data, 8, 20, 1-13, doi:10.1038/s41597-021-00802-4.

Mardones, M. and J. Rojas (2012). Procesos de remoción en masa inducidos por el terremoto del 27F de 2010 en la franja costera de la Región del Biobío, Chile, in Spanish, Rev. Geogr. Norte Gd., 53, 1, 57-74, doi:10.4067/S0718-34022012000300004.

Maringue, J., L. Mendoza, E. Sáez, G. Yañez et al. (2022). Geological and geotechnical investigation of the seismic ground response characteristics in some urban and suburban sites in Chile exposed to large seismic threats. Geological and geotechnical investigation of the seismic ground response characteristics in some urban and suburban sites in Chile exposed to large seismic threats, B. Earthq. Eng., 20, 1, 4895-4918, doi:10.1007/s10518-022-01401-3.

Melgar, D., T. Taymaz, A. Ganas, B. Crowell et al. (2023). Sub- and super-shear ruptures during the 2023 Mw 7.8 and Mw 7.6 earthquake doublet in SE Türkiye, Seismica, 2, 3, 1-10, doi:10.26443/seismica.v2i3.387.

Moreno, M., M. Rosenau and O. Oncken (2010). 2010 Maule earthquake slip correlates with pre-seismic locking of Andean subduction zone, Nature, 467, 1, 198-202, doi:10.1038/nature09349.

Mourhatch, R. and S. Krishnan (2020). Simulation of Broadband Ground Motion by Superposing High-Frequency Empirical Green's Function Synthetics on Low-Frequency Spectral-Element Synthetics, Geosci., 10, 9, 1-26, doi:10.3390/geosciences10090339.

Noda, A., T. Saito, E. Fukuyama and Y. Urata (2021). Energy-based scenarios for great thrust-type earthquakes in the Nankai trough subduction zone, southwest Japan, using an interseismic slip-deficit model, J. Geophys. Res. Sol. Ea., 126, 5, 1-20, doi:10.1029/2020JB020417.

Nweke, C. C., J. P. Stewart, R. W. Graves, C. A. Goulet et al. (2022). Validating predicted site response in sedimentary basins from 3D ground motion simulations, Earthq. Spectra, 38, 3, 2135-2161, doi:10.1177/87552930211073159.

Ohnaka, M. (2013). The physics of rock failure and earthquakes, Cambridge University Press, doi:10.1017/CBO9781139342865.

Ojeda, J., A. Akinci, E. Tinti, S. Arriola et al. (2021). Hybrid Broadband Strong-Motion Simulation to investigate the near-source Characteristics of the M6.5, 30 October 2016 Norcia, Italy Earthquake, Soil Dyn. Earthq. Eng., 149, 1, 1-16, doi:10.1016/j.soildyn.2021.106866.

Okubo, P. G. and K. Aki (1987). Fractal geometry in the San Andreas Fault System, J. Geophys. Res. Sol. Ea., 92, B1, 345-355, doi:10.1029/JB092iB01p00345.

Oral, E., J. P. Ampuero, J. Ruiz and D. Asimaki (2022). A Method to Generate Initial Fault Stresses for Physics-Based Ground-Motion Prediction Consistent with Regional Seismicity, B. Seismol. Soc. Am., 112, 6, 2812-2827, doi:10.1785/0120220064.

Pan, E. and B. Amadei (1995). Stress concentration at irregular surfaces of anisotropic half-spaces, Acta Mech., 113, 1, 119-135, doi:10.1007/BF01212638.

Pandit, B. I. and M. S. King (1979). The variation of elastic wave velocities and quality factor Q of a sandstone with moisture content, Can. J. Earth Sci., 16, 12, 2187-2195, doi:10.1139/e79-206.

Panza, G. F., F. Romanelli, F. Vaccari, L. Decanini et al. (2004). Seismic ground motion modeling and damage earthquake scenarios: a possible bridge between seismologists and seismic engineers, in Earthquake hazard, risk, and strong ground motion Y. T. Chen, G. F. Panza, Z. L. Wu (Editors), Seismological, Beijing, 323-349.

Paolucci, R., I. Mazzieri, C. Smerzini and M. Stupazzini (2014). Physics-Based Earthquake Ground Shaking Scenarios in Large Urban Areas, in Perspectives on European Earthquake Engineering and Seismology A. Ansal (Editor), Geot. Geol. Earthquake, 34, 1, 331-359, doi:10.1007/978-3-319-07118-3_10.

Pathier, E., E. J. Fielding, T. J. Wright, R. Walker et al. (2006). Displacement field and slip distribution of the 2005 Kashmir earthquake from SAR imagery, Geophys. Res. Lett., 33, 20, 1-5, doi:10.1029/2006GL027193.

Pérez, A., J. A. Ruiz, G. Vargas, R. Rauld et al. (2014). Improving seismotectonics and seismic hazard assessment along the San Ramón Fault at the eastern border of Santiago city, Chile, Nat. Hazards, 71, 1, 243-274, doi:10.1007/s11069-013-0908-3.

Pilz, M., S. Parolai, M. Stupazzini, R. Paolucci et al. (2011). Modelling basin effects on earthquake ground motion in the Santiago de Chile basin by a spectral element code, Geophys. J. Int., 187, 2, 929-945, doi:10.1111/j.1365-246X.2011.05183.x.

Rezaeian, S. and X. Sun (2014). Stochastic Ground Motion Simulation, in Encyclopedia of Earthquake Engineering M. Beer, I. Kougioumtzoglou, E. Patelli, I. Au (Editors), Springer, Berlin, Heidelberg, 1-15, doi:10.1007/978-3-642-36197-5_239-1.

Riesner, M., R. Lacassin, M. Simoes, R. Armijo et al. (2017). Kinematics of the active West Andean fold-and-thrust belt (central Chile): Structure and long-term shortening rate, Tectonics, 36, 2, 287-303, doi:10.1002/2016TC004269.

Rivera, F., T. Rossetto and J. Twigg (2020). An interdisciplinary study of the seismic exposure dynamics of Santiago de Chile, Int. J. Disast. Risk Re., 48, 1, 1-12, doi:10.1016/j.ijdrr.2020.101581.

Rojas, F., F. Naeim, M. Lew, L. D. Carpenter et al. (2011). Performance of tall buildings in Concepción during the 27 February 2010 moment magnitude 8.8 offshore Maule, Chile earthquake, Struct. Des. Tall Spec., 20, 1, 37-64, doi:10.1002/tal.674.

Saragoni, G. R., M. Lew, F. Naeim, L. D. Carpenter et al. (2010). Accelerographic measurements of the 27 February 2010 offshore Maule, Chile earthquake, Struct. Des. Tall Spec., 19, 8, 866-875, doi:10.1002/tal.673.

Schliwa, N. and A. A. Gabriel (2023). Equivalent Near-Field Corner Frequency Analysis of 3D Dynamic Rupture Simulations Reveals Dynamic Source Effects, Seismol. Res. Lett., 95, 2A, 900-924, doi:10.1785/0220230225.

Shimmoto, S. (2024). Source Parameter Scaling Relations for Shallow Crustal Earthquakes: Exploration With the Single Asperity Model, J. Geophys. Res. Sol. Ea., 129, 2, 1-28, doi:10.1029/2023JB027690.

Smith, E. (1986). The effect of crack front irregularity on the fracture toughness of brittle materials, Arch. Mech., 38, 1-2, 185-190, https://www.rcin.org.pl/publication/110311.

Somerville, P., K. Irikura, R. Graves, S. Sawada et al. (1999). Characterizing crustal earthquake slip models for the prediction of strong ground motion, Seismol. Res. Lett., 70, 1, 59-80, doi:10.1785/gssrl.70.1.59.

Song, C., S. Pujol and A. Lepage (2012). The Collapse of the Alto Río Building during the 27 February 2010 Maule, Chile, Earthquake, Earthq. Spectra, 28, 1, 301-334, doi:10.1193/1.4000036.

Song, S. G. and B. Duan (2023). Dynamic Rupture Models of the 2016 ML 5.8 Gyeongju, South Korea, Earthquake, Constrained by a Kinematic Rupture Model and Seismic Waveform Data, B. Seismol. Soc. Am., 114, 2, 710-725, doi:10.1785/0120230099.

Strasser, F. O. and J. J. Bommer (2009). Review: Strong Ground Motions – Have We Seen the Worst?, B. Seismol. Soc. Am., 99, 5, 2613-2637, doi:10.1785/0120080300.

Taborda, R. and D. Roten (2015). Physics-Based Ground-Motion Simulation, in Encyclopedia of Earthquake Engineering M. Beer, I. Kougioumtzoglou, E. Patelli, I. Au (Editors), Springer, Berlin, Heidelberg, 1-33, doi:10.1007/978-3-642-36197-5_240-1.

Tinti, E., E. Fukuyama, A. Piatanesi and M. Cocco (2005). A Kinematic Source-Time Function Compatible with Earthquake Dynamics, B. Seismol. Soc. Am., 95, 4, 1211-1223, doi:10.1785/0120040177.

Tinti, E., M. Cocco, E. Fukuyama and A. Piatanesi (2009). Dependence of slip weakening distance (Dc) on final slip during dynamic rupture of earthquakes, Geophy. J. Int., 177, 3, 1205-1220, doi:10.1111/j.1365-246X.2009.04143.x.

Vargas, G., Y. Klinger, T. K. Rockwell, S. L. Forman et al. (2014). Probing large intraplate earthquakes at the west flank of the Andes, Geology, 42, 12, 1083-1086, doi:10.1130/G35741.1.

Venegas-Aravena, P., E. G. Cordaro and D. Laroze (2022) Fractal Clustering as Spatial Variability of Magnetic Anomalies Measurements for Impending Earthquakes and the Thermodynamic Fractal Dimension, Fractal Fract., 6, 11, 1-13, doi:10.3390/fractalfract6110624.

Venegas-Aravena, P. (2023a). Heterogeneous self-arrested ruptures leading to spatial variability of radiated energy and Doppler effect of the observed corner frequency, J. Seismol., 28, 1, 187-208, doi:10.1007/s10950-023-10183-3.

Venegas-Aravena, P. (2023b). Geological earthquake simulations generated by kinematic heterogeneous energy-based method: Self-arrested ruptures and asperity criterion, Open Geosci., 15, 1, 1-20, doi:10.1515/geo-2022-0522.

Venegas-Aravena, P. and E. G. Cordaro (2023). Subduction as a Smoothing Machine: How Multiscale Dissipation Relates Precursor Signals to Fault Geometry, Geosci., 13, 8, 1-16, doi:10.3390/geosciences13080243.

Venegas-Aravena, P., J. Crempien and R. J. Archuleta (2024). Fractal Spatial Distributions of Initial Shear Stress and Frictional Properties on Faults and Their Impact on Dynamic Earthquake Rupture, B. Seismol. Soc. Am., 114, 3, 1444-1465, doi:10.1785/0120230123.

Venegas-Aravena, P. (2024). Past large earthquakes influence future strong ground motion: Example of the Chilean subduction zone, Nat. Hazards, 120, 1, 10669-10685, doi:10.1007/s11069-024-06651-9.

Venegas-Aravena, P. (2025). The Multiscale physics behind the Rikitake time, general friction law, and precursory-coseismic energy scaling, Multiscale Multidiscip. Mod. Exp. Des., 8, 139, 1-15, doi:10.1007/s41939-025-00728-z.

Venegas-Aravena, P. and D. Zaccagnino (2025). Large earthquakes are more predictable than smaller ones, Seismica, 4, 1, 1-16, doi:10.26443/seismica.v4i1.1568.

Vora, H. B. and J. K. Morgan (2019). Microscale Characterization of Fracture Growth and Associated Energy in Granite and Sandstone Analogs: Insights Using the Discrete Element Method, J. Geophys. Res., 124, 8, 7993-8012, doi:10.1029/2019JB018155.

Wang, D., C. Li, Z. Meng and H. Wang (2021). Vulnerability Analysis Based on Ground Motion Intensity Parameters, IOP Conf. S., Earth Env. Sci., 719, 1, 1-5, doi:10.1088/1755-1315/719/4/042003.

Wang, X. C., J. T. Wang, L. Zhang, S. Li et al. (2021). A Multidimension Source Model for Generating Broadband Ground Motions with Deterministic 3D Numerical Simulations, B. Seismol. Soc. Am., 111, 2, 989-1013, doi:10.1785/0120200221.

Xie, H. (1993). Fractals in Rock Mechanics, A. A Balkema Brookfield, Rotterdam, Netherlands, ISBN: 9789054101338.

Yañez, G., M. Muñoz, V. Flores Aqueveque and A. Bosch (2015). Gravity derived depth to basement in Santiago Basin, Chile: implications for its geological evolution, hydrogeology, low enthalpy geothermal, soil characterization and geo-hazards, Andean Geol., 42, 2, 147-172, doi:10.5027/andgeoV42n2-a01.

Yañez, G., N. Perez-Estay, J. Araya-Vargas, J. Sanhueza et al. (2020). Shallow Anatomy of the San Ramón Fault (Chile) Constrained by Geophysical Methods: Implications for its Role in the Andean Deformation, Tectonics, 39, 8, 1-21, doi:10.1029/2020TC006294.

Youssef, N. F., D. Tunick, F. Naeim, M. Lew et al. (2011). Performance of the Torre Bosquemar and Olas buildings in San Pedro de la Paz and the Pedro de Valdivia building in Concepción in the 27 February 2010 offshore Maule, Chile earthquake, Struct. Des. Tall Spec., 20, 1, 65-82, doi:10.1002/tal.670.

Zaccagnino, D. and C. Doglioni (2022). Earth's gradients as the engine of plate tectonics and earthquakes, Riv. Nuovo Cimento, 45, 1, 801-881, doi:10.1007/s40766-022-00038-x.

***CORRESPONDING AUTHOR: Patricio VENEGAS ARAVENA**,
Universidad Loyola Andalucía, Department of Engineering,
Avda. de las Universidades s/n, Dos Hermanas, 41704, Seville, Spain
e-mail: plvenegas@uc.cl